LEVEL

Dynamics of Laser Driven, Ablatively Accelerated Targets

JACOB GRUN

Department of Physics and Astronomy
University of Maryland
College Park, Maryland

May 8, 1981

DTIC
ELECTE
MAY 1 3 1981

A

NAVAL RESEARCH LABORATORY
Washington, D.C.

81 5 13 067

REPORT DOCUMENTATION PAGE	READ INSTRUCTIONS BEFORE COMPLETING FORM

1. REPORT NUMBER NRL Memorandum Report 4491	2 GOVT ACCESSION NO.	3. RECIPIENT'S CATALOG NUMBER

4. TITLE *(and Subtitle)* DYNAMICS OF LASER DRIVEN, ABLATIVELY ACCELERATED TARGETS*	5. TYPE OF REPORT & PERIOD COVERED Interim report on a continuing NRL problem.
	6. PERFORMING ORG. REPORT NUMBER

7. AUTHOR(s) Jacob Grun	8. CONTRACT OR GRANT NUMBER(s)

9. PERFORMING ORGANIZATION NAME AND ADDRESS University of Maryland College Park, Md. 20742	10. PROGRAM ELEMENT, PROJECT, TASK AREA & WORK UNIT NUMBERS 47-0859-0-2

11. CONTROLLING OFFICE NAME AND ADDRESS Naval Research Laboratory Washington, D.C. 20375	12. REPORT DATE May 8, 1981
	13. NUMBER OF PAGES 90

14. MONITORING AGENCY NAME & ADDRESS*(If different from Controlling Office)*	15. SECURITY CLASS. *(of this report)* UNCLASSIFIED
	15a. DECLASSIFICATION/DOWNGRADING SCHEDULE

16. DISTRIBUTION STATEMENT *(of this Report)*

Approved for public release; distribution unlimited

17. DISTRIBUTION STATEMENT *(of the abstract entered in Block 20, If different from Report)*

18. SUPPLEMENTARY NOTES

Work sponsored by Office of Naval Research and Department of Energy.
*Present address: Mission Research Corporation, Alexandria, VA

19. KEY WORDS *(Continue on reverse side if necessary and identify by block number)*

Ablation plasma, ablation momentum, ablation pressure, mass ablation rate, ablation velocity, pendulum, double-foils, target velocity, ablation depth, laser-plasma interaction, ballistic pendulum, laser spot-size effects, pellet-shell velocity

20. ABSTRACT *(Continue on reverse side if necessary and identify by block number)*

The characteristics of ablation plasma from planar targets, driven by long Nd:glass laser pulses (4 nsec, 10^{14} W/cm^2), and the velocity of the ablatively accelerated targets are experimentally studied.

Ablation plasma diagnostics include arrays of time-of-flight ion collectors, plasma calorimeters, and ballistic pendula which directly measure the plasma velocity, energy, and momentum. The ballistic pendula have been tested and calibrated in the experimental environment. A novel

(Continued)

DD $_{1\ JAN\ 73}^{FORM}$ 1473   EDITION OF 1 NOV 65 IS OBSOLETE
S/N 0102-014-6601

20. ABSTRACT (Continued)

double-foil technique has been developed and used to study the velocity of the accelerated target.

Using measurements of plasma energy, velocity, and momentum, we determine the scaling with irradiance and the absolute magnitudes of the ablation pressure, velocity and ablation depth (or mass ablation rate). These results are insensitive to laser spot-size effects that may introduce error under some experimental conditions. They imply that the hydrodynamic efficiency and initial thickness of targets accelerated to fusion velocities are weak and strong functions of absorbed irradiance respectively. Thus, target thickness and irradiance may be varied as necessary to alter the pellet-aspect-ratio or to increase laser nonuniformity smoothing with only small changes in hydrodynamic efficiency. We have determined that the accelerated target is composed of a high pressure, high density region preceeded by a low pressure, low density plasma. We have measured the velocity of the high density region and found that it agrees with target velocities predicted from the ablation parameters using a simple rocket model. We accelerated targets over distances many times their own thickness to velocities of 100 km/sec with no apparent breakup. These dense target velocities are close to the implosion velocities required of hollow fusion-pellet shells.

Accession For
NTIS CRA&I
DTIC TAB
Unannounced
Justification

By
Distribution/
Availability Codes
Avail and/or
Dist Special

CONTENTS

DYNAMICS OF LASER-DRIVEN, ABLATIVELY

ACCELERATED TARGETS

INTRODUCTION

Search for a method of controlling thermonuclear fusion reactions to produce electric power continues for about three decades. Development of such a method would permit tapping of the practically unlimited energy locked-up in naturally occurring fusionable nuclei and free mankind from its dependence on fossil fuels: In an era of rapidly dwindling energy resources this research becomes imperative. One fusion technique now being considered is the laser-driven, ablative implosion of hollow pellets made of fusionable fuel. In this scheme, powerful laser beams ablate material from the hollow pellet surface creating high pressures that implode the pellet in a process analogous to a rocket. If it could be arranged for the imploding pellet to converge inward with sufficient symmetry, sufficient kinetic energy, and on a low adiabat; then, upon convergence the pellet fuel is compressed long enough for thermonuclear fusion reactions with a net energy gain to occur. This energy would be extracted and used to run the turbines of a conventional electric power plant.

The present work is part of a larger integrated and ongoing experiment studying the feasibility of the fusion scheme briefly sketched above. Our aim is to verify that planar targets, modeling sections of a hollow pellet, may be accelerated to the velocities required for fusion, and to measure the ablation parameters that help define an operating regime for a practical fusion scenario. For this purpose, new diagnostics had to be developed. Then quantitative measurements of the dense target velocity and ablation plasma parameters under various target, laser-spot size, and irradiance conditions were made. These topics will be discussed in the sections that follow:

Section I   describes what we measure, and why;

Section II   reviews past theoretical and experimental contributions;

Section III   describes the methods and diagnostics used in these experiments; and

Section IV   presents our results and discusses their implications.

Section I

WHAT WE MEASURE AND WHY

The basic goal of fusion research is to confine a plasma of hydrogen isotopes in which fusion reactions with a net energy gain take place. Regardless of the confinement scheme used, two conditions must be satisfied: first, the reacting plasma must be heated so that the rate of thermonuclear energy production exceeds the rate of energy loss due to bremstrahlung radiation;[a,1] second, for a net energy gain (fusion energy/thermal energy > 1) the product of plasma density and the reaction time must be greater than 10^{14} sec/cm^3 (Lawson's criterion).[2] In inertial confinement fusion, researchers attempt to exceed these criteria by heating a highly compressed deuterium-tritium (DT) plasma ($\sim 10^{26}$ ions/cm^3) and confining it with its own inertia for a few picoseconds.[3] For this technique Lawson's criterion is equivalent to a condition on the compressed plasma density ρ_c and radius R_c, $\rho_c R_c \geq 0.2$ gm/cm^2.[b] Just exceeding this criterion, however, is not sufficient for commercial fusion application since the thermonuclear energy produced must also make up for the inefficiency of the driver as well as the energy wasted in the driver-plasma coupling, compression, and ignition processes. Inertial confinement fusion concepts require $\rho_c R_c$ to be about 3 gm/cm^2. Below, I will briefly describe the particular fusion scheme that motivates the present work and relate our measurements to it.

A. Fusion with Ablatively Driven, Hollow Pellets

The pellet type whose feasibility we are studying[4] consists of a hollow, spherical (few mm diameter) DT shell coated with a material called an ablator (Fig. 1a). By analogy with a rocket,

---

[a] For deuterium-tritium plasma reactions, $D + T \rightarrow {}^4\mathrm{He}(3.5\ \mathrm{MeV}) + n\ (14.1\ \mathrm{MeV})$, and if the reaction products are captured by the plasma, the heat energy is ≥ 3 KeV

[b] We assume that the reaction time τ_c is given by $\tau_c = R_c/4C_s$, where C_s is the speed of sound. We also assume that $C_s \approx \sqrt{10/3}\ V_{th}$ where the thermal velocity $V_{th} \approx 6 \times 10^7$ at 10 KeV. For the origin of these relations see the article by G.S. Fraley, et al. in reference 1

the DT shell may be thought of as the rocket payload, and the ablator as the rocket fuel. Powerful lasers heat the ablator whose rapid evaporation supplies the thrust to implode the hollow shell towards the center of the sphere (Fig. 1b). If the implosion is sufficiently energetic, symmetric and the shell sufficiently cool, the DT stagnates as it reaches the center and is compressed to a high density. The compression should be done such that a small central region ($\rho_h R_h \sim .3$ gm/cm^2 at 10 keV) of the compressed DT is shock heated to the temperature required for fusion reactions, with little extra investment in energy. The fusion reactions that begin at the core rapidly spread thru the rest of the compressed DT fuel as alpha particles from the reactions deposit their energy in the rest of the pellet thereby propagating the thermonuclear burn from (Fig. 1c).

Among the parameters we consider are:

a. Shell Velocity

For the hollow pellet envisioned in Ref. 4," the deuterium shell must be compressed to ~ 3000 times solid density. To supply the energy necessary for such compression ($\sim 2 \times 10^7$ J/gm) the shell velocity must be about 200 km/sec. It is important to verify experimentally whether acceleration to such high velocity with the required uniformity and efficiency is possible. Our measurements of planar target velocities, modeling pellet shells, will be described in the following sections.

b. Ablation Pressure

If the hollow pellet fusion scheme is to work, some contradictory requirements will have to be reconciled. For example, during the acceleration phase the dense imploding shell is pushed by a less dense ablation plasma without. Since this is not a minimum energy

---

"The pellet parameters are: Pellet gain = 1000, burn efficiency = 40%, implosion efficiency = 14%, fuel mass $\approx 10^{-3}$ gm, specific energy = 2×10^7 J/gm.

DT-FUEL SHELL

ABLATOR

(a) PELLET
CROSS SECTION

IMPLODING FUEL
ABLATION
LASER LIGHT

(b) ABLATIVE
IMPLOSION

CENTRAL IGNITION
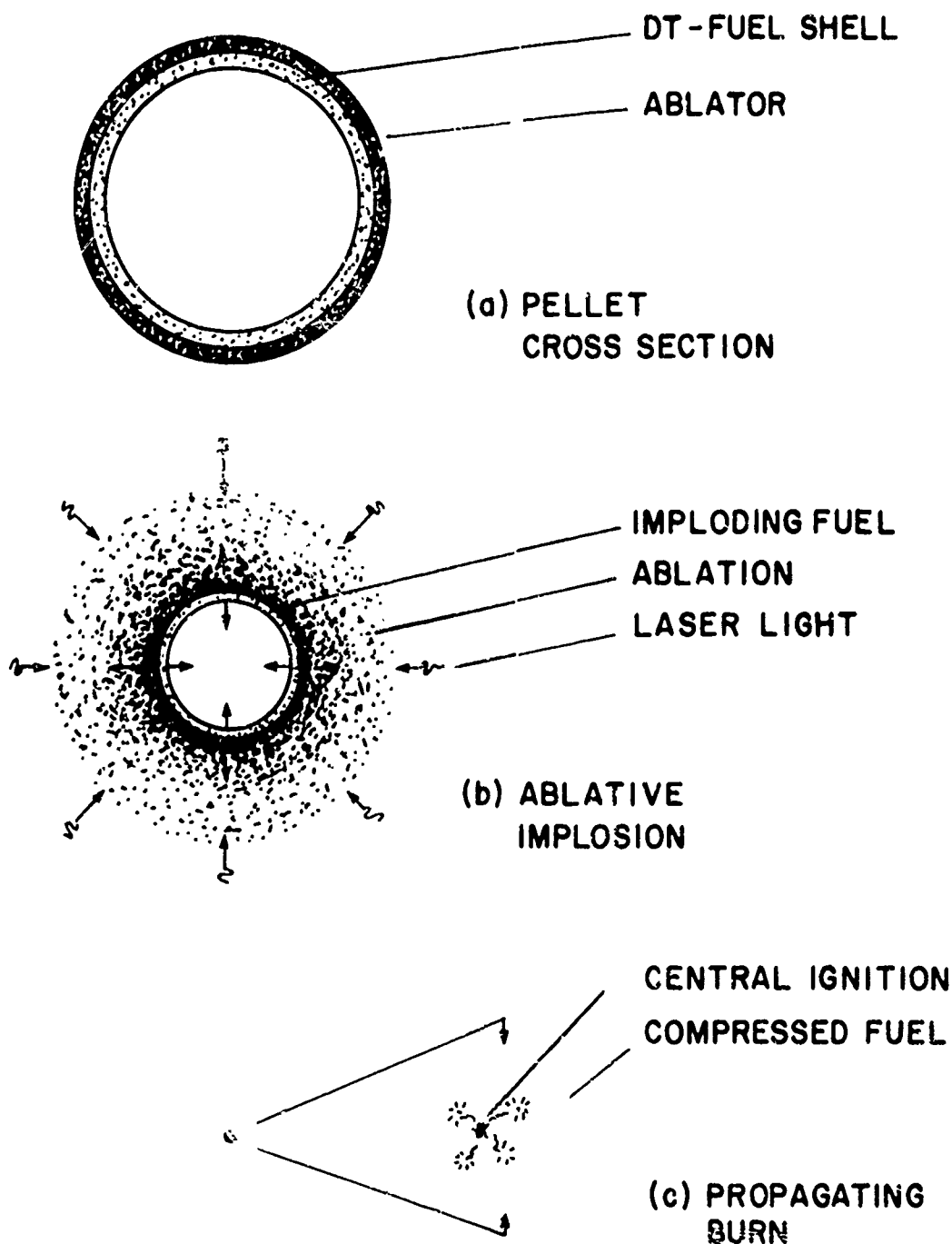
COMPRESSED FUEL

(c) PROPAGATING
BURN

Fig. 1.1 — A simplified diagram showing a hollow fusion pellet
(a) before, (b) during, and (c) after implosion

5

configuration, the DT shell and ablator material will tend to mix and brake up the pellet. To limit the development of this (Raleigh-Taylor) instability.[5], the shell should be accelerated to its final fusion velocity in the shortest possible time. This requires high pressures and, therefore, high laser intensities. However, irradiance cannot be raised without limit. Eventually undesirable effects of high irradiance will appear, limit the energy available for compression, and in addition make the shell even harder to compress. Known effects include Brillouin backscatter[6] that reduces the absorption of laser light, production of fast electrons[7][9] that would heat the DT fuel prematurely, as well as production of fast ions and inhibited thermal transport[7][8][11] that reduce the efficiency of acceleration.

We must verify whether an irradiance regime that avoids non-uniform implosions, avoids the undesirable effects of high irradiance, and is consistent with accelerating the shell to the required velocity exists.[12] For this reason we have measured the ablation pressure and its scaling with irradiance. Also, comparing experimental and theoretical scaling laws aids our understanding of the ablation mechanism.

c. Ablation Velocity and Mass Ablation Rates

Ablation velocity is an important quantity influencing the hydrodynamic efficiency of the hollow pellet implosion. Using a rough analogy, the ablating plasma and pellet shell may be thought of as products of a "decay" in which one particle transforms into two components—a light one and a heavy one. In this situation most of the decay energy ends up in the light product, although the momentum of the products is shared equally. In the fusion case too, most of the absorbed laser energy (E_a) ends up as the kinetic energy of the ablation plasma $\frac{1}{2} M u^2$ where M is the total ablated mass and u its mean velocity. Since the momentum transferred to the pellet shell is given by $-2 E_a/u$, for a given absorbed energy low velocity ablation ions generate high pressure more efficiently than fast ions. Scaling laws that relate ablation velocity to

the hydrodynamic efficiency of acceleration may be derived from a simple rocket model.[13]

Consequently, knowing the ablation velocity and its scaling with irradiance is important when

searching for a parameter space in which the pellet can operate. Knowing the mass ablation

rate (or mass ablation depth) also makes it possible to infer the thickness of a pellet shell that

can be accelerated to fusion velocity with the required efficiency. We have measured ablation

velocities, mass ablation depths, and their scalings with irradiance. The results will be shown in

Section IV.

Section II

REVIEW OF THEORY AND EXPERIMENTS

In part A of this section the theory of ablative acceleration is presented. Emphasis is placed on the basic physics of the ablation process and of the moving shell under ideal conditions. The description is not exhaustive, but it does describe current thinking on the subject. Scaling laws relevant to our experiment are summarized in this part. Measurements related closely to our own are reviewed in part B. Of necessity, important work dealing with effects such as laser-beam absorption, laser-beam uniformity, or target preheat is not discussed. The reader is urged to consult Refs. 1-3 and references therein for information on these subjects.

A. Theory

a. Ablation

Schematics of the electron temperature and density profiles of plasma during the ablation process are sketched in Fig. II.1.[4,5] The laser-beam penetrates the plasma from the right being absorbed on the way until a critical density n_c (10^{21} cm^{-3} for a Nd-glass laser), where any remaining laser energy may be reflected or resonantly absorbed.[6] For the long duration, low intensity laser pulses considered here (3-4 nsec, $< 10^{14}$ W/cm^2) plasma flow establishes a relatively long scale-length, relatively low temperature absorption region. In this environment the electron-ion collision frequency is high enough to provide efficient absorption by inverse-bremsstrahlung.[7,8] Most of the laser energy is probably absorbed by this process.[1]

Much of the absorbed energy—especially near critical density—conducts down the steep temperature gradient towards the cooler target surface where it heats up and ablates surface
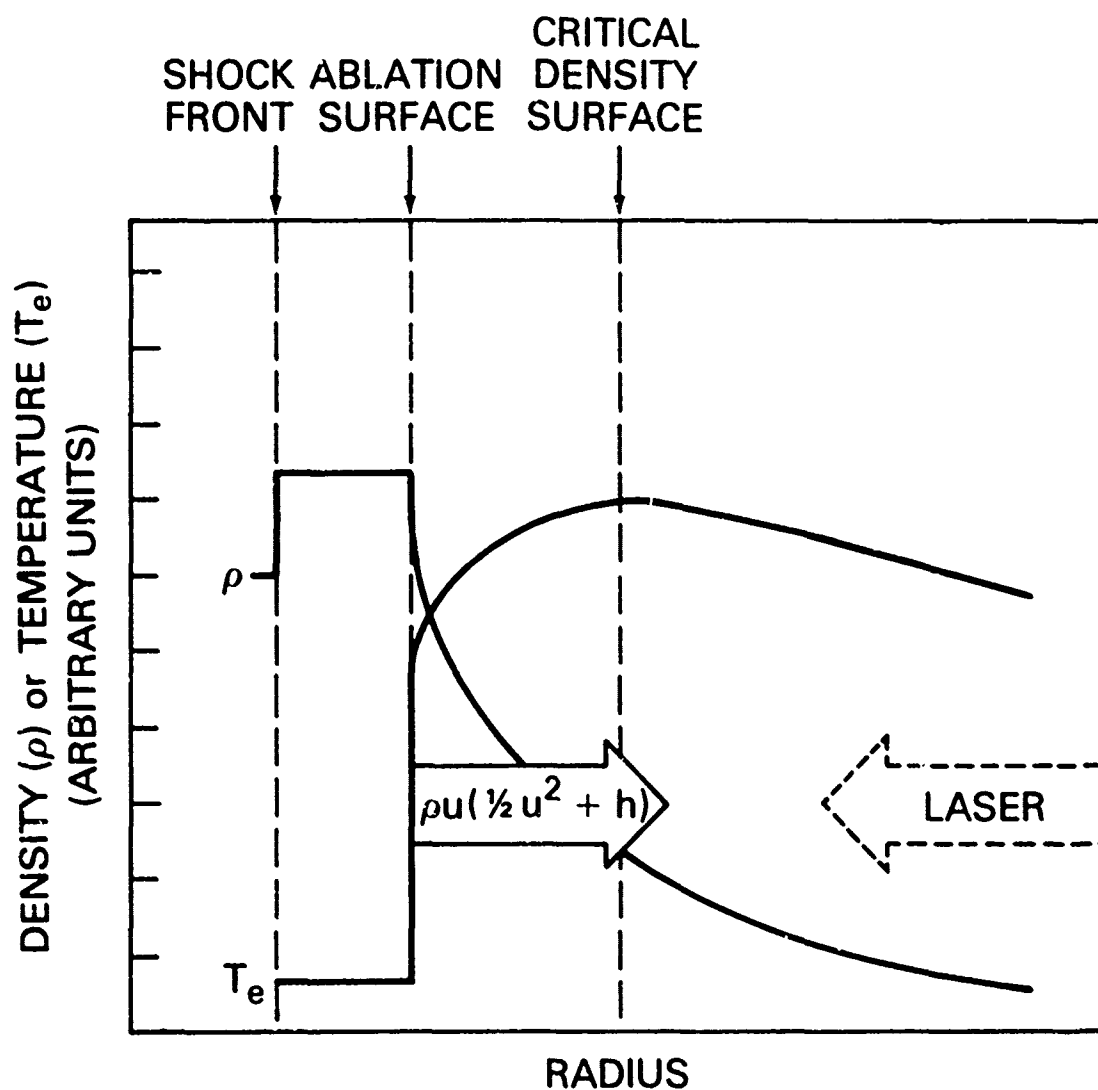
8

Fig. II.1 — Schematic of the density (ρ) and electron temperature (T_e) profiles of an ablatively driven target; u is the ablation velocity and h the specific enthalpy.

material. This ablating material (plasma) expands from the surface and, in so doing, exerts a pressure which compresses and eventually moves the target; a shock can be generated causing the density step depicted in Fig. II.1. The flow of ablated plasma thru the critical density surface and towards the laser also replenishes the plasma in the absorption region. In particular, if this flow occurs on a time scale much faster then changes in the incident irradiance—something assumed in most theories—a self-consistent regulation cycle that establishes and maintains the profiles in Fig. II.1 is expected to set in. For example, if the ablation rate should for some reason slightly decrease, lack of plasma in the absorption region will move the critical density closer to the ablation surface. This will result in absorption closer to the target, the temperature near the critical surface would rise, temperature gradient (Fig. II.1) would steepen, and the ablation rate will go back up. If instead the ablation rate should increase, this process is reversed. Assuming such a steady or quasi-steady ablation structure, ablation plasma properties are commonly described by these steady state equations:

$$\nabla \cdot [\rho \overline{u}] = 0 \qquad \text{(mass conservation)} \qquad \text{(II.1)}$$

$$\rho(\overline{u} \cdot \nabla)\overline{u} = -\nabla \mathcal{P}_p \qquad \text{(Newton's Law)} \qquad \text{(II.2)}$$

$$\nabla \cdot \left[\rho \overline{u} \left(\frac{1}{2}u^2 + h\right) + \overline{q}\right] = \rho Q \quad \text{(Energy conservation)} . \qquad \text{(II.3)}$$

where $\rho, \overline{u}, \mathcal{P}_p$, and h are the plasma density, velocity, pressure, and specific enthalpy respectively; Q is the energy deposited in the plasma per unit mass per unit time, and $\overline{q}$ is the thermal heat flux expressed by the minimum of $\overline{q} = (-k\nabla T_c)$ or $\overline{q} = \left\{-f\rho_c \left[\frac{kT_c}{m_c}\right]^{3/2} \left[\frac{\nabla T_c}{|\nabla T_c|}\right]\right\}$; the latter expression is valid in the free streaming limit.

This is the basic picture assumed in most ablation theories; individual authors differ in the way they treat various details of the problem. Simple theories (Kidder,[9] Caruso and Gratton[10]), which are in planar geometry, neglect details of the absorption and energy transport to the ablation layer. They also assume that all of the absorbed energy supports the expansion of the abla-

tion plasma, and that the underdense plasma expands with sonic velocity (also called the Chapman-Jouget hypothesis).[9] Some theories (Jarboe et al.[11]) assume sonic flow at the critical surface and some (Ahlborn et. al.[12, 13]) eliminate the sonic flow hypothesis altogether.

In practice, no laser-target experiment is truly planar. Plasma from flat targets irradiated by finite-diameter laser spots, for example, expands laterally; the expansion becoming significant when the plasma reaches a distance comparable to the laser spot diameter. Plasma from uniformly irradiated pellet targets expands spherically. Nevertheless, if the sphericity of the plasma flow becomes significant only after the hydrodynamic parameters reach their final, or almost final values (ie., when the ablation to critical surface distance $<<$ pellet radius or laser spot diameter), then a planar theory may still be able to describe the experiment. Thus, experiments using large pellets or large laser spots may be described with a planar theory. However, experiments using small pellets or small laser spots may be better described by a spherical theory.

Divergent plasma flow from planar targets was considered by Puell[14] who treated plasma hydrodynamics in planar geometry using a model similar to Refs. 9 and 10, but considered plasma expansion when calculating absorption of laser light and the temperature at the sonic radius. (The sonic radius is the radius at which the plasma makes a transition from subsonic to supersonic flow.) Scalings of ablation param... rs with irradiance in spherical geometry were determined by Nemchinov[15] who neglected thermal transport. Scaling of the mass ablation rate was determined by Gitomer et al.[16] who included thermal transport but assumed that the sonic radius does not vary with irradiance. Inhibited thermal conductivity in spherical geometry (at irradiances higher than ours) was considered by Rosen et al.[17] and Max et al.[18]

Scalings with irradiance of ablation pressure, ablation velocity, and mass ablation rate predicted by these theories are shown in Table II.1. Most of the theories give similar results.

Table II.1 — Comparison of theoretically derived scaling laws: Table entries are the exponents of $\alpha \equiv I_a^n$ where α is either the ablation pressure $\mathscr{P}_\perp$, ablation velocity $u_\perp$, ablation depth d, or the mass ablation rate $\dot{m}_j$; and I_a is the absorbed irradiance. Theories referred to may be found in refs. 9 thru 18.

THEORY	$\mathscr{P}_\perp$	$u_\perp$	d or $\dot{m}$
KIDDER	.75	.25	.50
CARUSO	.75	.25	.50
AHLBORN	.78*	.22*	.56*
JARBOE	.66**	.33**	.33**
PUELL	.78	.22	.56
NEMCHINOV	.78	.22	.56
GITOMER			.56
MAX	.57	.09	.48

*$\eta^{\pm 1/9}$, $\eta^{2/9}$ IN AHLBORN'S EXPRESSIONS HAVE HERE BEEN TREATED AS CONSTANTS. η IS THE ABSORPTION FRACTION.

**JARBOE ET AL. DERIVE EXPLICITLY A RELATION FOR $u_\perp$ ONLY. TO GET THE OTHER TWO QUANTITIES WE USED THE RELATIONS $\mathscr{P}_\perp \propto n_c u_\perp^2$ AND $\dot{m} \propto n_c u_\perp$ IMPLIED BY HIS THEORY; n_c IS THE CRITICAL DENSITY.

However, fixing the sonic plasma exhaust at critical density[11] and not letting the exhaust density vary with irradiance changed the scalings noticeably. Inclusion of inhibited thermal transport[18] changed the scalings also.

b. Physics at the Ablation Surface-Target Interface

It was explicitly recognized by some authors[8,14] that the Chapman-Jouget hypothesis may be invalid but it was often used because it simplified the ablation model. This hypothesis and the physics at the ablation surface-solid target interface will be reviewed below.[19]

The sharply rising temperature profile in Fig. II.1 may be viewed as a stationary, infinitely steep heat front burning its way into the solid target. Just as is the case with shocks, the propagation of such heat fronts depends not only on local parameters such as density but also on external conditions remote from the heat front such as energy absorption mechanisms or plasma thermodynamics. Three modes of heat front propagation are recognized depending on the absorbed intensity I_a, enthalpy h of the heated plasma, and the density ρ of the cool material preceeding the step[13,20] $[h = h(I_a/\rho)]$.

Mode (1): The heat front velocity is subsonic with respect to both the cool plasma in advance of the step and the hot plasma in back of the step. Under these conditions, the thrust of the hot plasma near the step surface drives a shock wave that overtakes the heat step and moves ahead of it. This is the behavior pictured in Fig. II.1. It occurs when h is high and I_a/ρ is low.

Mode (2): The heat front velocity is supersonic with resp   . to both the cool plasma in advance of the step and the hot plasma in back of the step. Under these conditions no "message" can be transmitted from the hot plasma to the cool material, so that no pressure precursors can develop. The heat front burns directly into an uncompressed

13

target. Once the heat front passes, the pressure gradients associated with the thrust of the accelerated plasma lose their momentum to a subsequent rarefaction wave. This occurs when h is low and I_a/ρ is high.

Mode (3): The heat front is sonic with respect to the hot plasma in back of the step. Here the pressure and heat fronts move together. This occurs when $h \propto (I_a/\rho)^{2/3}$. Any deviation from this condition causes modes (1) or (2) to appear.

Mode (3) is the so called Chapman-Jouget detonation. It is the naturally occuring mode in chemical detonations when an unstable chemical is locally activated by a shock wave. The resulting chemical reaction gives off heat at a rapid rate. The heat, in turn, maintains the shock wave—which detonates more material to produce more heat and so on. In this closely coupled, self-sustaining cycle the heat and pressure fronts move together. But, when the heat source is a laser the cycle described above does not exist so that the Chapman-Jouget detonation would occur only for a special set of conditions. In fact, absorption by inverse-bremsstrahlung may not be consistent with the Chapman-Jouget process.[12] Interestingly, Ahlborn and Key[12] found that in the ablation process the velocity of the heat front is only slightly subsonic. This may account for the good agreement between his theory and theories that use the Chapman-Jouget hypothesis.[12]

c. Pellet-Shell Motion

When a particle decays into a heavy and a light component the light component carries most of the energy but momentum is shared equally. A shell accelerated by an ablating plasma behaves similarly i.e. most of the absorbed laser energy is carried by the plasma but the plasma momentum is balanced by a shock wave in the denser shell material. Consequently, once this shock wave equilibrates, shell kinematics may be described using momentum conservation laws—in a manner analagous to a rocket.[21] Shock equilibration mechanisms, spall, or shock

14

heating are, of course, ignored in such analysis. A planar geometry rocket with a cold exhaust was used recently to model the results of an ablative acceleration experiment.[22] The model was found to be in agreement with experiment once a correction for the angular divergence of the exhaust (i.e., blowoff plasma) in the experiment was made. A rocket with a hot exhaust[23] (and no geometrical corrections) explains ablative acceleration experiments as well.

Planar rocket models may describe the early stages of a fusion pellet implosion. However, later in the implosion phenomena such as an increasing pressure at the pellet surface due to the decreasing pellet surface area, or shocks reflecting from the pellet center alter this simple picture. Spherical convergence effects were treated by Kidder, and Ashby.[24]

B. Experiment

Ablative acceleration experiments in which both the ablation plasma and the accelerating shell are studied in an integrated manner have begun recently.[25-27] Instead of imploding hollow pellets, these experiments accelerate planar targets meant to simulate a section of a pellet shell before convergence effects become dominant. Planar targets have the advantage that both the hot (outer) and cool (inner) surfaces are easily accessible to diagnostics. However, large diameter laser spots (≥ 1 mm) are necessary to obtain quantitative results in this type of experiment since two-dimensional effects at the edges of smaller spots may distort the results. Finite-laser-spot effects and our measurements of ablation plasma and target properties will be discussed in detail in Sections III and IV. Below, we review observations reported in the literature.

a. Some Words on Diagnostics

The diagnostics used to measure ablation properties include time-of-flight ion collectors to measure plasma speed, plasma calorimeters to measure plasma energy, and pendula to measure

plasma momentum. Ablation pressures were also inferred by observing shock speeds in optically clear targets,[28] and mass ablation rates (or depths) determined with layered—target techniques.[1,29] When evaluating the experimental literature, the following diagnostic peculiarities must be kept in mind.

- In Sec. IV we will show that it is important to keep the laser-spot-diameter large ($\geq$ 1 mm). More importantly, changing irradiance in a parameter study by focusing down the laser beam should not be done without caution. Doing so alters the irradiation spotsize changing the amount of energy escaping thru the focal spot periphery[30] and the distance between the ablation and critical surfaces. This may introduce unwanted error. Focusing down the laser beam also changes the spatial profile of the irradiance and the nature and intensity of any hot spots in the beam. Layered-target experiments which are sensitive to the shape of the irradiance profile may be especially affected by this.

- When plasma ions strike a pendulum collector they can stick, "bounce off" its surface, or sputter material from it. The reflected or sputtered material, though of low energy,[31] generates recoil momentum that can be as large as the momentum of the incident ions. Pendula calibrations must take this into account. Note also that low energy but high momentum plasma, such as may originate from regions beyond the focal-spot, would also be sensed by a pendulum. Since the momentum contributed by such plasma would be irrelevant to laser fusion, its existence—or lack of it—must be verified. These issues will be discussed in Sec. III.

- Ion collectors measure currents passing a point far removed from the irradiated target so that the ion time-of-flight is much longer than the time of its

16

initial acceleration. Unlike in short, high irradiance laser pulse work,[32] ion collectors in the ablative regime measure a single sharp peak[33] so that their use as time-of-flight detectors is legitimate. However, the ablation velocity distribution is affected by laser spot size as will be shown in Sec. IV.

b. Ablation Experiments

The formation and expansion of blowoff plasmas from targets irradiated by long (> 1 nsec) laser pulses were studied in the middle sixties with the advent of multijoule ruby lasers ($\lambda = 0.69\mu$m).[34-36] Scaling of ion kinetic energies[34,35] and of the relative number of blowoff ions[36] with intensity was inferred from ion collector traces. These observations were in agreement with planar ablation theory. In later work with infrared lasers ($\lambda = 1.05\mu$m) quantitative measurements and scalings with intensity of blowoff ion velocities and mass ablation rates were obtained[37] (see Sec. IV). The charge state of ablation ions was also measured and found to be in good qualitative agreement with the theory.[33]

In an early measurement, time-resolved pressure generated by a 5-nsec glass laser pulse was inferred at a single irradiance by watching the velocity of an opaque front (believed to be a shock wave) in the irradiated target.[28] Others inferred the scaling of average pressure with irradiance by measuring the response of a pendulum when it was struck by the accelerated target debris.[38] In this experiment target momentum was inferred from the pendulum motion. The target area over which the momentum acts was inferred theoretically and pressure was determined using the formula: pressure = momentum/(area × laser duration.) A similar pendulum technique was used to measure the momentum of the ablation (blowoff) plasma.[39] Our measurements infer ablation pressure from the plasma blowoff momentum also,[37,40] but are distinguished from the previous work in that the area from which the momentum arrives is *experimentally* determined and the contribution of sputter or reflection from the pendulum surface is included in its calibration. Details will be presented in Sec. III.

c. Target Velocity Experiments

Although measurements on ablatively accelerated targets have just recently begun, the experimental techniques are improving rapidly. In some of the early experiments,[26] time-of flight ion collectors were a common diagnostic of target motion. These detectors collect target debris passing a point far removed from the target so that the debris time-of-flight is much greater than the time of its initial acceleration. Consequently, the technique is subject to criticism that the target during the crucial acceleration and post-acceleration phases remains unobserved. The acceleration and motion of planar targets were also studied thru observations of the shadow cast by the moving target when it is illuminated by an optical probing beam.[26,27] In this method, though, the internal structure of the accelerating target (shadow) is also unobserved. Particularly, it is hard to tell whether the moving shadow edge is cast by the dense bulk of the target or by lower density plasma preceding and obscuring the dense part of the target. More recently, space and time resolved velocity profiles of targets during the early stages of acceleration were obtained by bouncing a short duration probe beam off the target's rear surface and observing the resulting doppler shift.[41] Our latest experiments permit the velocity of the dense "bulk target" material and the qualitative nature of the shadow cast by the target to be determined with a unique double-foil technique. Dense targets moving at velocities of 100 km/sec have been observed.[37] This technique and experimental results will be described in detail in Secs. III and IV.

Section III

INSTRUMENTS AND METHODS

The apparatus used to study ablatively accelerated targets consists of a powerful laser driver, a target irradiation facility, and associated diagnostics. An overview of the laser, the irradiation facility, and common diagnostics will be given in parts A and B below. Then, the diagnostics and methods peculiar to our experiment will be described.

A. Laser Driver

The driver for these experiments is the NRL Pharos II Nd:glass laser, capable of delivering over 600 Joules on target in a 3-5 nsec pulse.[1] A schematic of this laser is shown in Fig. III.1. The master oscillator is a neodymium-yttrium-lithium-fluoride (Nd:YLF), passively Q-switched unit lasing at a 1.054μm wavelength. This is followed by a single pass, 6.4 mm aperture Nd:YLF preamplifier and two Nd:phosphate glass rod amplifiers (diameters $\phi = 23$ mm, and 32 mm) that boost the oscillator energy 800 fold. The laser beam is then split into two components and each component is further amplified by a 45 mm aperture rod amplifier; optically relayed thru two disk amplifiers ($\phi = 67$ mm, and 105 mm); and then relayed again into the target irradiation area and onto the focusing lens. For most of the shots in this work only one beam of this laser was used. The soft aperture[1] shown in the diagram was installed after our experiment was complete.

To obtain as uniform an illumination as possible over a large area, the planar targets used in these experiments are placed between the point of best focus and the near field of a 1.2 meter, f/6, aspheric focusing lens. The target normal is tilted 6° with respect to the laser axis to protect the laser from back reflection and to make the target normal accessible to diagnostics.
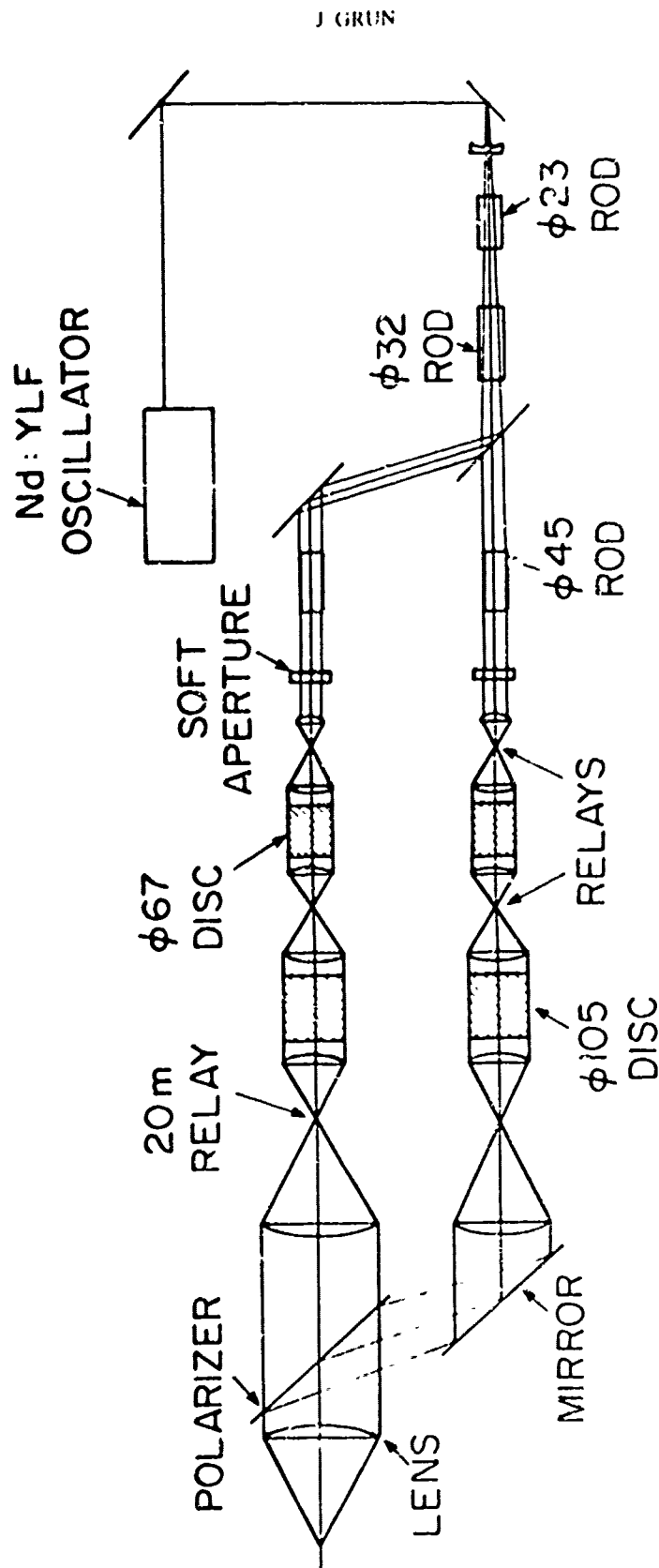
Fig. III.1 — Optical layout of the Pharos II laser with isolation stages deleted for clarity. The symbol φ refers to the diameter of the amplifier aperture. For most of the shots in this work only the upper laser chain was used. The soft aperture in the diagram was installed after our work was complete.

Unless otherwise stated in the text, irradiance is varied by reducing the gain of the disk amplifiers so that the spacial irradiance profile does not change significantly. Typical irradiance profiles in the target plane, measured with a thin-film ablation technique,[2] are shown in Fig. II.2. The focal distributions are fairly uniform and free of astigmatism, irradiance variation in the central ringed part of the distribution is about $\pm 50\%$.

B. Target Irradiance Facility

The target facility of the laser-plasma interaction group at NRL contains the final alignment, focusing, and diagnostic stages of the Pharos II laser, a chamber that contains the target, a computerized data acquisition system, and our plasma/target diagnostics. These are adequately described in the literature[1] so only an overview is given here. Diagnostics especially relevant to this work are described in parts C and D.

The laser beam, discussed in part A, is optically relayed from the laser building and onto the target chamber focusing lens. Incident and back reflected laser light is monitored utilizing reflections off appropriately placed beam-splitter surfaces. Laser energy, temporal history, and the spatial irradiance profile in the target plane (see Fig. III.2) are measured on each shot. The laser energy is measured with an Apollo calorimeter;[4] a fast, ~ 300 psec, MRD 510 PIN diode coupled to a Tektronix 7104 oscilloscope measures the temporal history. The targets to be irradiated are placed in a chamber and positioned with a precise XYZ translator. Planar geometry is chosen for our experiments so that both the front and the rear sides of the target are readily accessible to diagnostics. The chamber itself, shaped like a 60 cm diameter octahedron-rhombi cube, is evacuated to about 50 microtorr for all the shots in this paper. Most plasma and target diagnostics are placed in, or are attached to, this chamber. Other diagnostics view the plasma from the outside. The diagnostics include:
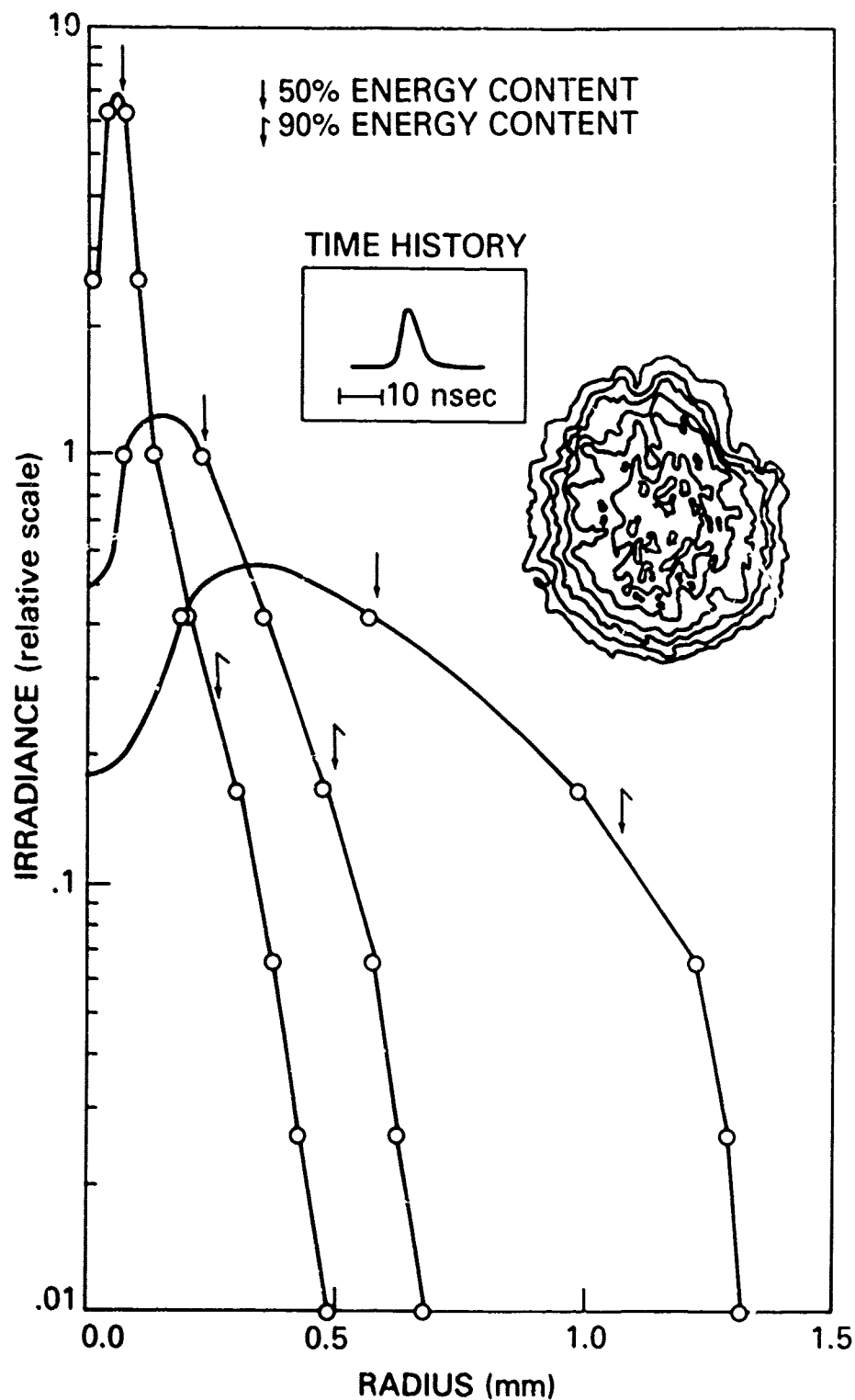
Fig. III.2 — Azimuthally averaged radial intensity profiles at the target plane. Focal spot radius in varied by moving the focusing lens. Arrows indicate radii within which 50% or 90% of the energy is contained. Inserts show the temporal behaviour of the laser pulse and constant irradiance contours of a 1-mm diameter laser spot.

- arrays of time-of-flight ion collectors, plasma calorimeters, and ballistic pendula to directly measure the plasma or target velocity, energy, and momentum respectively.

- a box-calorimeter to measure laser absorption.[3][5]

- an optical probing beam utilized for several purposes, e.g., multiple frame shadowgraphy,[3,6] interferometry,[3,6] doppler shift soundings,[7] and double foil experiments.[8]

- a Hadland Imacon 675 streak camera with S-1 and S-20 tubes used in the double foil experiments.[8]

- astigmatic spectrographs used to measure the temperature of the target rear.[9]

- x-ray diagnostics such as: an array of seven PIN diode - filter combinations to measure 1-10 KeV emission spectra;[10] four filter-scintillator-PMT x-ray detectors which cover the 10-50 KeV region; a PIN diode - Be filter device to time resolve 1-2 KeV x-ray emission;[3,6] an XUV spectrograph;[3,6] x-ray pinhole cameras; a spectroheliograph.

- and others.

C. Ion Diagnostics and Methods

Figure III.3 shows the setup used for measuring hydrodynamic parameters of the ablation plasma and of the accelerated target. The laser beam enters from the figure's right. Part of the beam is diverted by a beam splitter and used to measure the laser beam energy, time history, and the spacial irradiance distribution in an equivalent focal lens plane.[11] The remainder is focused by a 1.2 meter aspheric lens to irradiate a planar target positioned in the chamber with the aid of a telescope and an imaging vidacon. Shadowgraphy and interferometry are also used in conjunction with this experiment (measurements by J. A. Stamper).

INCIDENT LASER BEAM

3-4 nsec
1.05 μm
<600 J

LASER BEAM
DIAGNOSTICS

SHADOW GRAPHY
INTERFEROMETRY

LASER
PROBE
BEAM

BALLISTIC PENDULUM
MINICALORIMETER (PARTICLES)
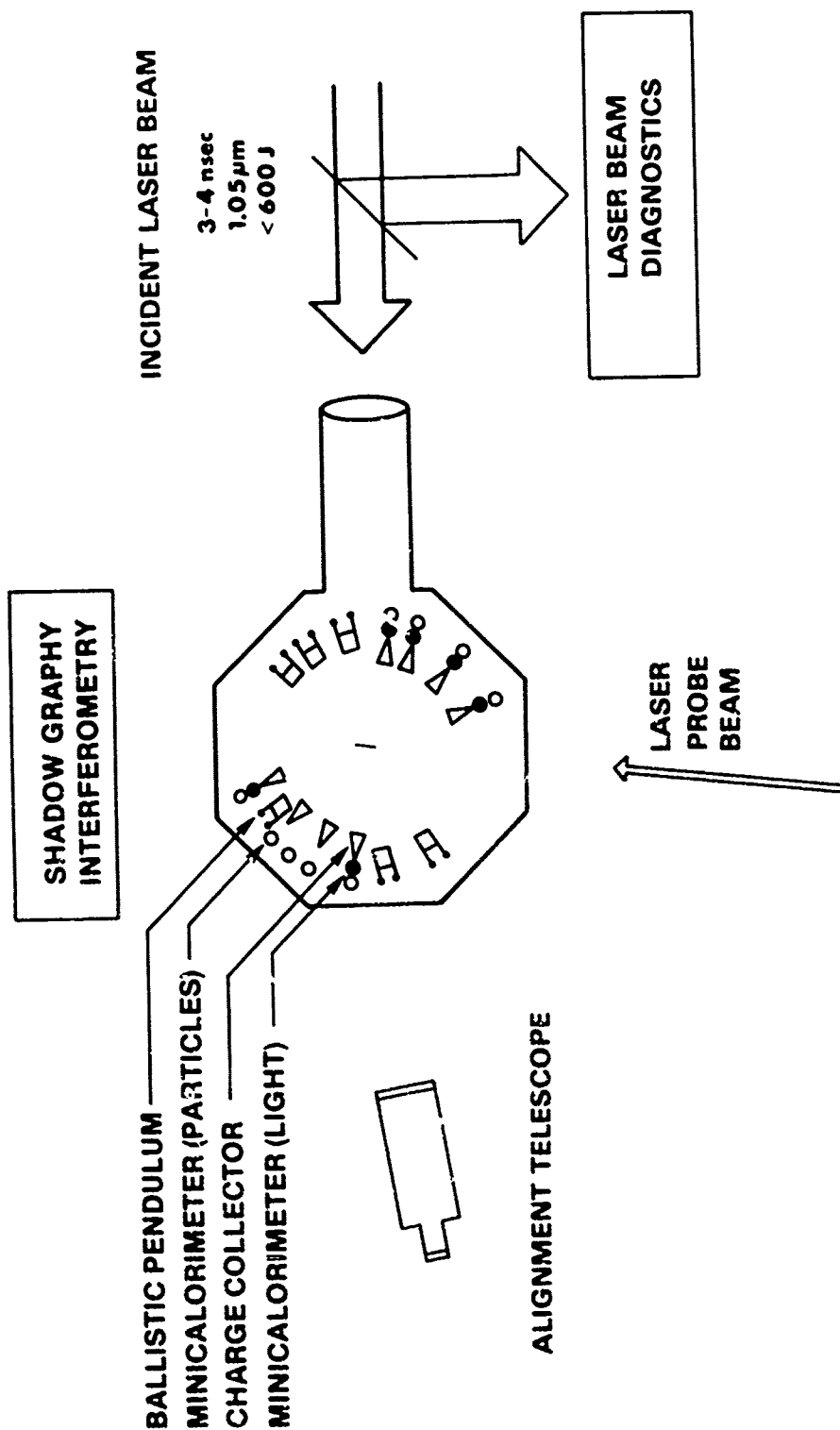CHARGE COLLECTOR
MINICALORIMETER (LIGHT)

ALIGNMENT TELESCOPE

Fig. III.3 — Experimental setup used to measure the ablation plasma or target energy, velocity, and momentum

The targets themselves are either thin, wide polystyrene foils [(CH)$_n$: 2-40 μm thick, ~3 mm wide], or thin polystyrene disks [0.3-1.2 mm in diameter]. In Section IV we will explain the need for both types of targets. Angular distributions of velocity, energy, and momentum are measured with arrays of time-of-flight ion collectors, plasma calorimeters, and ballistic pendula arranged around the chamber periphery. From these distributions mass ablation rates, ablation pressures and other quantities are inferred. These measurements will be presented in Section IV. Below, the devices themselves are described. The in-situ tests and calibration of the ballistic pendulum, not yet done in other laboratories, are described in detail.

a. Time-of-Flight Ion Collectors

Asymptotic ion velocities are obtained from measurements of ion current a known distance from the target surface. A schematic of an ion collector used for such measurement is shown in Fig. III.4a. The device consists of a flat copper collector plate biased to −150 volts with respect to its case and the chamber ground. Expanding plasma enters the detector through a small hole and a copper mesh. When the plasma comes within a few Debye lengths [$\lambda_D = (kT_e/4\pi n_e e^2)^{1/2}$] of the collector plate the ions and electrons are separated. The electrons, whose kinetic energy is on the order of 1 volt, are repelled to the earth ground; but the ions whose energy (~10 KeV for carbon) is much greater than the bias voltage and neutrals are not affected and strike the collector. To verify that good ion-electron separation does indeed take place, the bias voltage was reduced by a factor of 3 for a few shots—with no significant change in signal.

When plasma ions or neutrals strike the collector surface, a fraction of their kinetic and potential energy is transferred to the electrons of the collector metal.[12][13][14] If this energy is greater than the work function of the collector some (secondary) electrons escape its surface
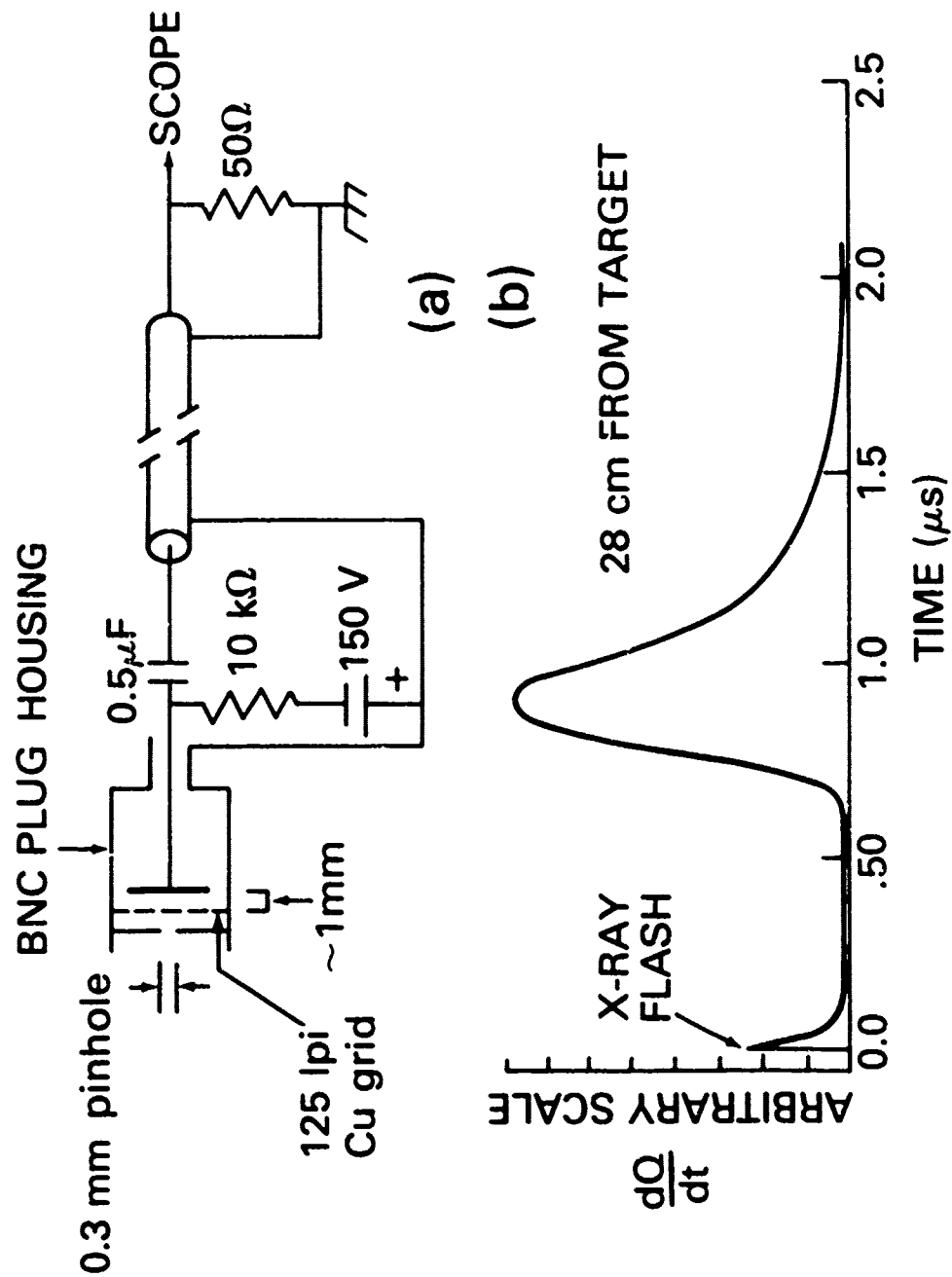
25

Fig. III.4 — (a) Schematic of an ion collector. (b) Ion collector trace from a detector placed about 28 cm from the target surface at an angle of 2° to the target normal.

and are repelled to the earth ground. Thus, if for each ion of charge state Z_j, γ_j secondaries are emitted, the collector current $\frac{dQ}{dt}$ is given by

$$\frac{dQ}{dt} = \frac{d}{dt} \sum_j e(Z_j + \gamma_j)N_j. \tag{III.1}$$

where N_j is the number of ions of charge state j and e is the electric charge. An example of an ion trace is shown in Fig. III.4b. The first small "blip" is caused by x-rays or ultraviolet light ejecting electrons from the collector surface as the laser strikes the target. This blip provides the initial time marker for time-of-flight analysis. An important feature of this trace is that it is *singly peaked* and *highly monoenergetic*. For instance the time-of-flight velocities at the FWHM points of the trace are within 15% of the peak velocity—the FWHM energies are within 30% of peak energy.[a] Therefore, we assume that the charge state Z_j and secondary electron coefficient γ_j are approximately constant over the charge collector trace and simplify Eq. (III.1) to read:

$$\frac{dQ}{dt} = e(Z + \gamma) \frac{dN}{dt}. \tag{III.2}$$

Then, from the current of an ion collector a distance s away from the target we may conveniently calculate the time averaged, asymptotic ion velocity:

$$\bar{u} \equiv \frac{\int \frac{dN}{dt} \frac{s}{t} dt}{\int \frac{dN}{dt} dt} = \frac{\int \frac{dQ}{dt} \frac{s}{t} dt}{\int \frac{dQ}{dt} dt}. \tag{III.3}$$

The velocity $\bar{u}$ is lower but close to the velocity of the ion trace peak. Note that since we use only the time-of-flight information exact values of the ion charge state Z or secondary electron coefficient γ need not be known—only the approximate constancy of these quantities over a sharply peaked, highly monoenergetic trace is assumed.

b. Plasma Calorimeters

The angular distribution of ion energy is measured with minicalorimeter pairs arranged around the target[15][16][17] (Fig. III.5a). The sensing element of each calorimeter consists of a

---

[a]Observation of even more monoenergetic traces will be discussed in Section IV

thin tantalum disk ($\sim$1.2 mil thick, $\sim$60 mil diameter) with 1 mil chromel-constantin thermo-couple wires spot welded to its rear. The other ends of these wires are attached to two small posts of a connector which serve as electrical contacts and a temperature reference for the ther-mocouple. When energy in any form is absorbed by the tantalum disk its temperature is raised producing a voltage signal at the thermocouple reference junction. In our experiment tempera-ture changes on the order of 1°K are produced yielding voltage signals of about 60μV. This voltage is amplified by a gain 1000 amplifier and read out on an oscilloscope (Fig. III.5b). The output impedance of the thermocouple junction is about 3Ω. A typical energy measuring unit consists of two minicalorimeters placed side by side. In one calorimeter the tantalum sensor faces the plasma directly and measures all incident ion, electron, x-ray, and light energy. The other calorimeter is covered with a pyrex glass window that eliminates ions, electrons, and x-rays but passes visible and near infrared light wavelengths. The difference in the signals from the two detectors is attributed to ion energy — x-ray[18] and electron energy being very small in comparison.

Sensitivity of the calorimeters to light energy was measured using a 1.06 μm wavelength light source. Sensitivity to ion energy was calculated from the known properties of tantalum and the thermocouple[a] assuming that all of the incident ion energy is absorbed. In reality, some of the energy delivered by ions is lost due to mechanisms such as ion backscatter, sputter-ing,[12] or secondary electron emission.[12,13] To estimate this loss we[b] placed a large tantalum plate 19 cm from the target surface and located two plasma calorimeters so that one (14 cm from target) measures the energy/area of the incident plasma and the other (17 cm from tar-get) measures the energy/area reflected or sputtered from the tantalum plate (Fig. III.6). Assuming that no energy loss at the calorimeter surface takes place, the ratio of the signals in the two calorimeters multiplied by $(19/14)^2$ (to account for the relative spacial ion distribution

---

[a] Thermocouple sensitivity $= 60 \mu$V/°K at 300°K. $C_\gamma = 6.06$ cal/mole °K, $\rho = 16.6$ gm/cm^3
[b] Measurement by B H. Ripin

(a)

CM

Ta disk   (b)   .22μf

200 kΩ pot

100Ω

741

Scope

1 mil
Chromel-Constantin
thermocouple

100Ω
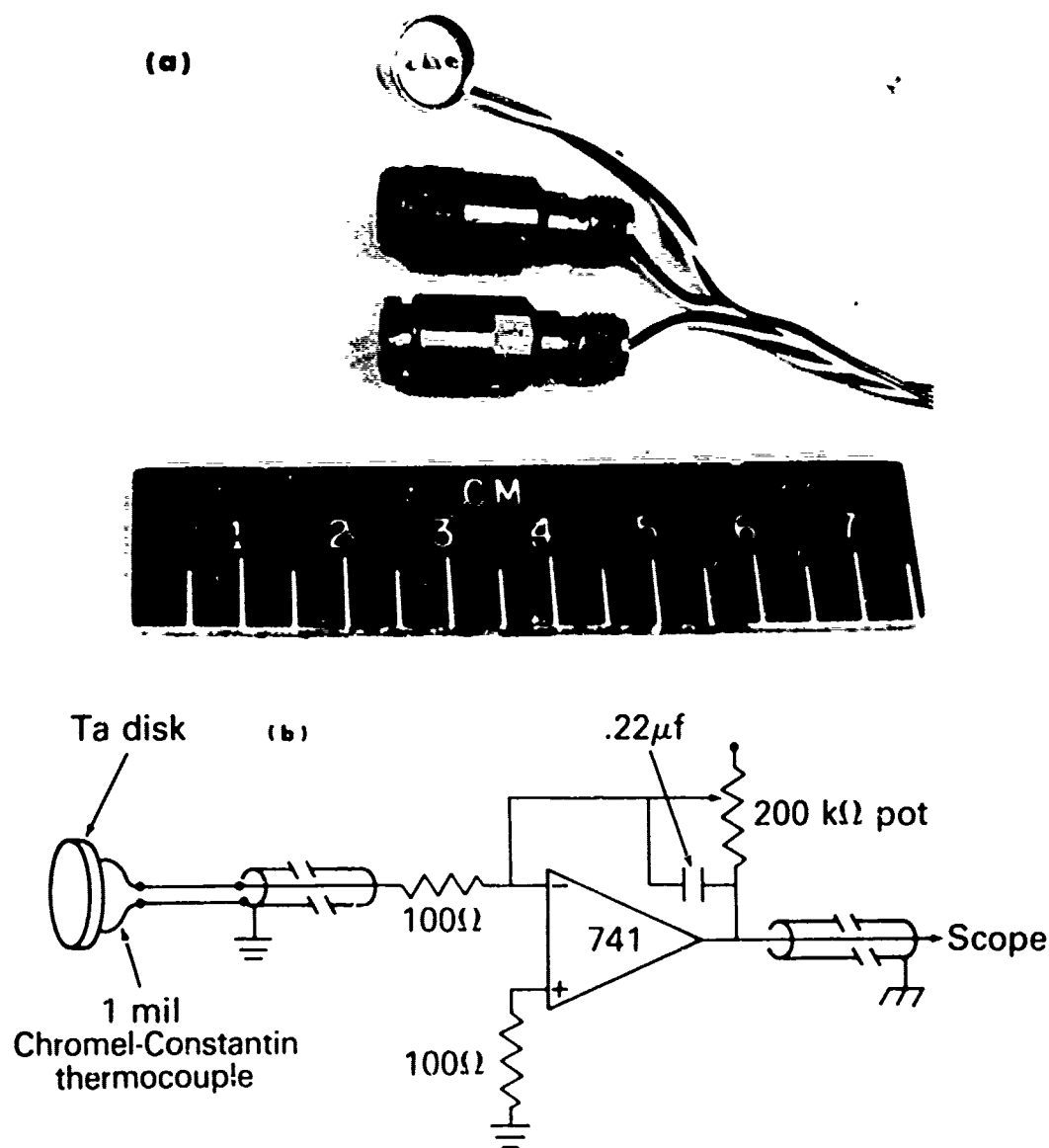
R-013

Fig. III.5 — (a) Photo of minicalorimeters (b) Minicalorimeter electronics.

29

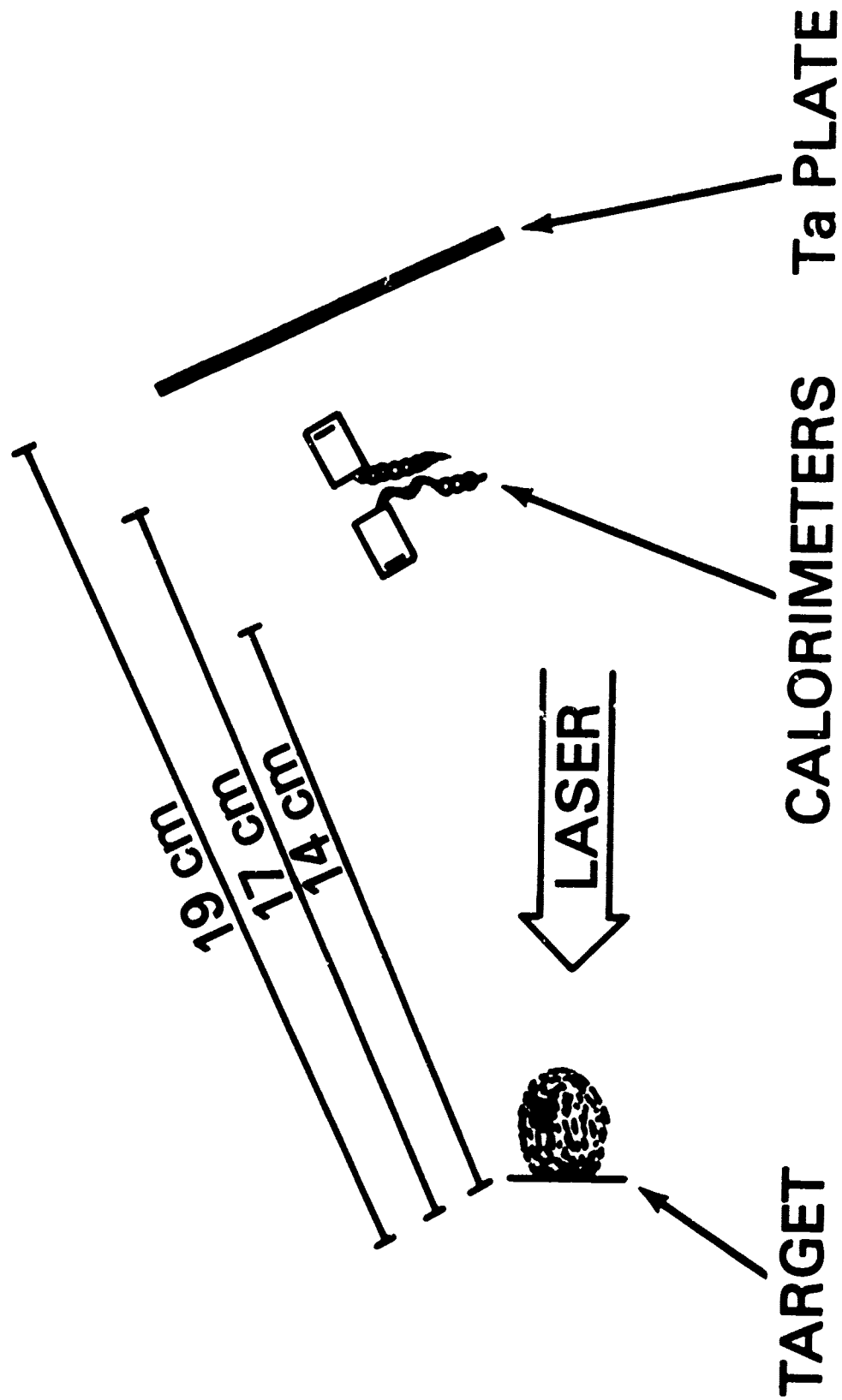TARGET LASER CALORIMETERS Ta PLATE

19 cm 17 cm 14 cm

Fig. III.6 — Setup to estimate fraction of incident plasma energy not absorbed by a tantalum surface.

at the incident energy detector and the tantalum plate surfaces) approximates the fraction of

incident energy not absorbed at the surface. This fraction at an irradiance of 10^{13} W/cm^2 is 3%.

When we placed pyrex windows on the calorimeters signals in both diminished greatly showing

that the contribution of light energy is negligible. However, since the sputtered or reflected

material has an angular distribution that scatters energy into and out of the solid angle viewed

by the reflection calorimeter, the actual fraction of energy not absorbed may be higher than the

3% estimated above.

c. Ballistic Pendula

The pendulum is a conceptually simple device that has been used in the laser-plasma

interaction context to determine the impulse transferred to irradiated targets[19-23] and the

momentum of the ablation plasma.[21] These experiments are configured so that the pendulum,

placed some distance in front or behind the irradiated target, intercepts the ablation plasma or

target debris—or the irradiated target is attached to the pendulum itself. In either case, the

impulse of the material impacting the pendulum is determined from the amplitude or the velo-

city of its swing; these have been measured by just looking at the pendulum, using a position

transducer, or a velocity sensitive pick-up coil.[21] Despite the apparent simplicity such use of

pendula is viewed with skepticism by many experimentalists. Their apprehension is easy to

understand: The pendulum is a mechanical, time integrating device that may be affected by

extraneous mechanisms due to the electrically noisy environment that normally exists in the

chamber during a shot. For example. Coulomb forces between a pendulum (if it became

charged through photoionization for instance) and the target or chamber walls could produce

pendulum deflection that could be misread as plasma or target momentum. Reflection or

sputter of material from the pendulum surface could also produce extraneous deflections. In

addition, the pendulum cannot distinguish between momentum from the laser-target interaction

region and irrelevant momentum (if any) produced outside the interaction region by energy

leaking through the focal-spot periphery. If the targets are very thick, momentum formed by the laser-target interaction cannot be distinguished from the momentum of materials ejected from the deep, shock-formed crater that remains after the shot.

Nevertheless, the pendulum *is* a simple device that measures momentum directly—*if* the above reservations are adequately addressed. In the parts that follow we will describe pendula we have built to measure the plasma and target momenta, determine the ablation pressure, and examine the validity of the pendulum technique.

(c.1) Design and Bench Calibration

We built two types of ballistic pendula: one type designed to carry a target, the other designed to be placed far from the target (~ 30 cm) so as to intercept ablation plasma or target debris. The target bearing pendulum is shown in Fig. III.7. It consists of an elongated plastic structure (1×10 cm, 4.5 gm) that has four triangular cavities machined into its middle. These cavities are designed to view the 2π-sr in back of the thin foil targets attached to their faces and to capture all of the accelerated target debris. There are four cavities on one pendulum so that four sequential shots can be taken without removing the pendulum from the evacuated target chamber. The pendulum pivot is made of a thin blade edge resting in cylindrical groves of the aluminum suppor. structure. The amount of friction in this pivot configuration is very small as evidenced by the long decay time of the pendulum swing. (No evidence of decay in 10 cycles). Pendulum motion is detected by a pick-up coil,[21] one end of which is glued rigidly to the bottom of the pendulum structure while the other is free to swing in a 3 mm gap between the poles of a permanent 3 KG magnet. The pickup coils are made of 200-1000 turns of 1 mil insulated copper wire. The remote pendula that detect ablation plasma or target debris consist of thin mylar or brass 25×40 mm collecting surfaces suspended from a blade pivot (as above)

32
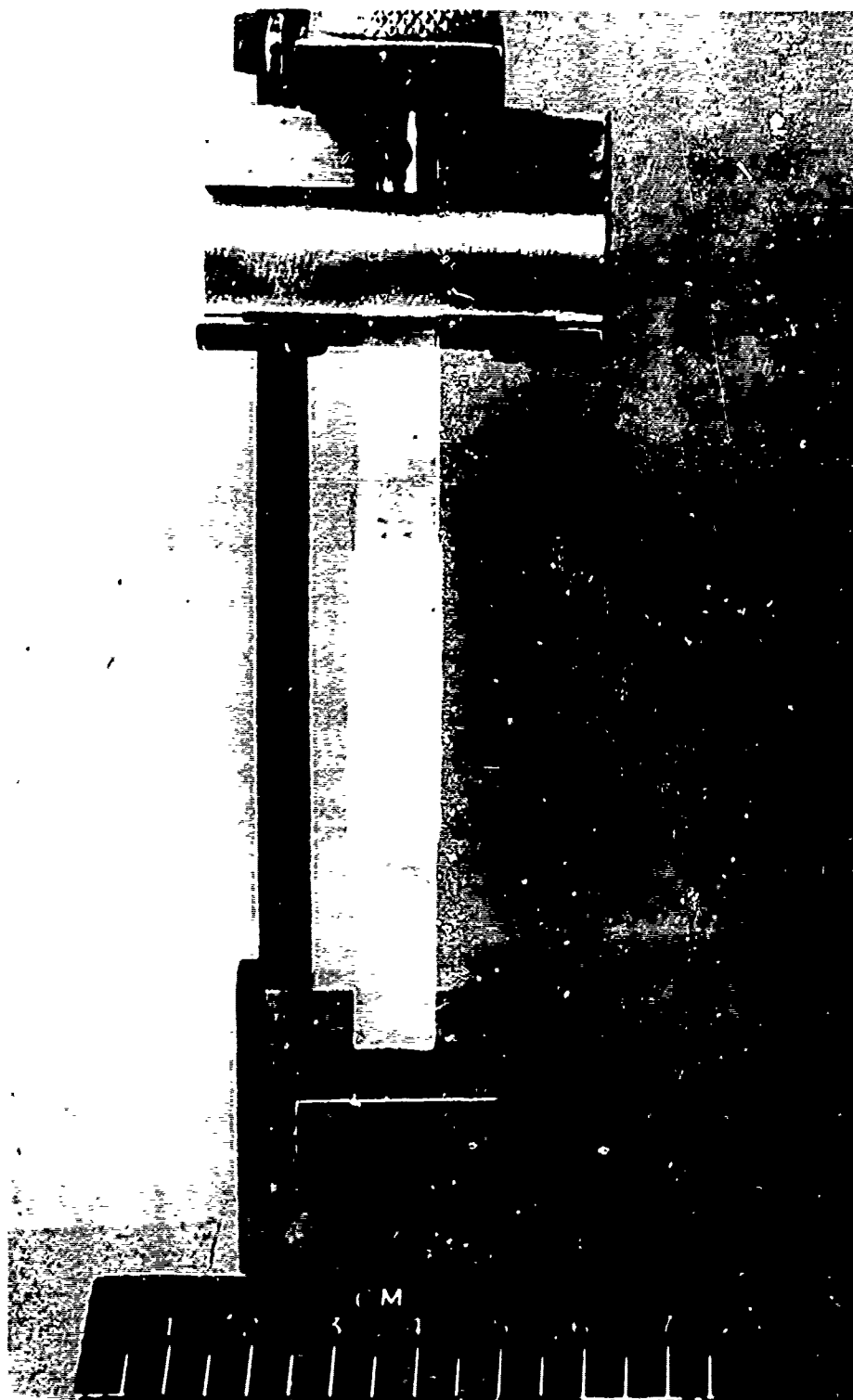
R-009

Fig III 7 — Target bearing pendulum

or by two thin nylon fishing lines. (The latter suspension method is inferio᾽ since it permits the pendulum to wobble about the vertical axis.) Motion of these pendula is also detected with a pick up coil.

When a pendulum is struck it swings at its natural frequency (2-3 Hz in our case) and induces an EMF in the pick up coil. The magnitude of the induced voltage is related to the momentum with which the pendulum was struck through the following equations (see Fig. III.8):

$$V_{pp} = 2na\, v_c\, B/c \qquad \text{(Faraday's Law)} \qquad (III.4)$$

$$pl = I v_c /r \qquad \text{(Momentum Conservation)} \qquad (III.5)$$

$$\nu^2 = Mgd/4\pi^2 I \qquad \text{(Frequency of Physical Pendulum).} \qquad (III.6)$$

where: V_{pp} is the peak to peak induced voltage. n is the number of turns in the pick-up coil, a is the length of coil in the magnetic field, v_c is the speed of the coil in the magnetic field, B is the magnetic field strength, c is the speed of light, p is the momentum that struck the pendulum at a distance l from the pivot, I is the moment of inertia of the pendulum, r is the distance from the pivot to the part of the coil that is in the magnetic field, M is the pendulum mass, g is the gravitational acceleration constant, and d is the distance from the pivot to the pendulum center of mass. All the units are Gaussian.

Combining (III.4), (III.5), and (III.6) we obtain:

$$p\ (\text{dyne-sec}) = 1.2 \times 10^6 \frac{Md}{nBral\nu^2}\ V_{pp}(mV\ ). \qquad (III.7)$$

All of the parameters in (III.7) are easily measured permitting a convenient and reliable bench calibration of the pendulum.

As a precaution against arithmetic error we suspended a small soft wax bob (~ 0.05 gm) from a thin thread ($\sim .004$ gm), raised the bob 1 cm and released it to swing and make an inelastic collision with our pendulum. The voltage induced in the pendulum coil agreed with that
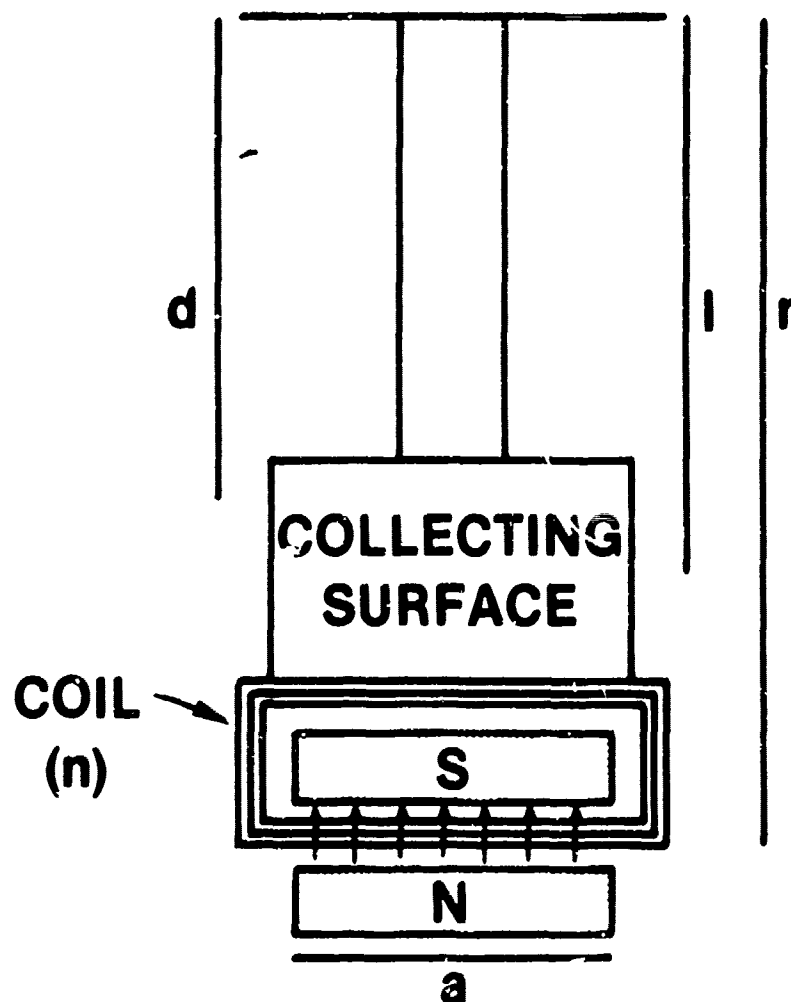
Fig. III.8 — Schematic of a remote pendulum. The symbols a, n, d, l, r are the length of coil in the magnetic field, number of turns in the coil, distance from pivot to center of mass, distance from pivot to location at which pendulum is struck, and distance from pivot to that part of the coil that is in the magnetic field.

expected from Eq. (III.7) to within 8%. The sensitivity of our pendula ranges from 7 to 34 mV/dyne-sec, depending on the details of construction. The lowest measurable momentum is determined by chamber and building vibrations that couple into or near the natural mode of the pendulum. In our laboratory such vibrations are equivalent to $\sim 5 \times 10^{-3}$ dyne-sec—which corresponds to a $\sim 2 \mu$m horizontal displacement of the pick-up coil.

The readout electronics for the voltage induced in the coil (Fig. III.9) consist of a high impedance buffer followed by a gain 100 amplifier and a low pass filter that eliminates electrical or vibrational noise frequencies higher than 10 Hz. A remotely controlled, solid state switch is used to damp out pendulum motion preceding a shot.

(c.2) In-Situ Checkout

Many of our measurements are made with an array of six ballistic pendula placed around the target at $-19°$, $-33°$, $-50°$, $145°$, $162°$, and $235°$ to the target normal. Although the pendula are bench calibrated, there is no guarantee that they will continue to function as "advertised" under experimental conditions—or that the momentum they do measure is relevant to laser fusion. In this part questions dealing with the in-situ functioning of the pendulum array are addressed. Absolute pendulum calibration will be discussed in part c.4.

The remote pendula function in a noisy environment. During a shot, for example, the target potential may rise to a few kilovolts,[24] and the chamber is full of electromagnetic noise that is easily picked up by a wire antenna. The pendula surfaces are also bombarded by charged particles and plasma UV or x-ray radiation.

Do phenomena other than ion impact cause pendulum deflection?

To see, we shielded (with mylar) the front of the pendulum collecting surface from direct ion impact and radiation—and noted no significant pendulum response during a shot. We also used
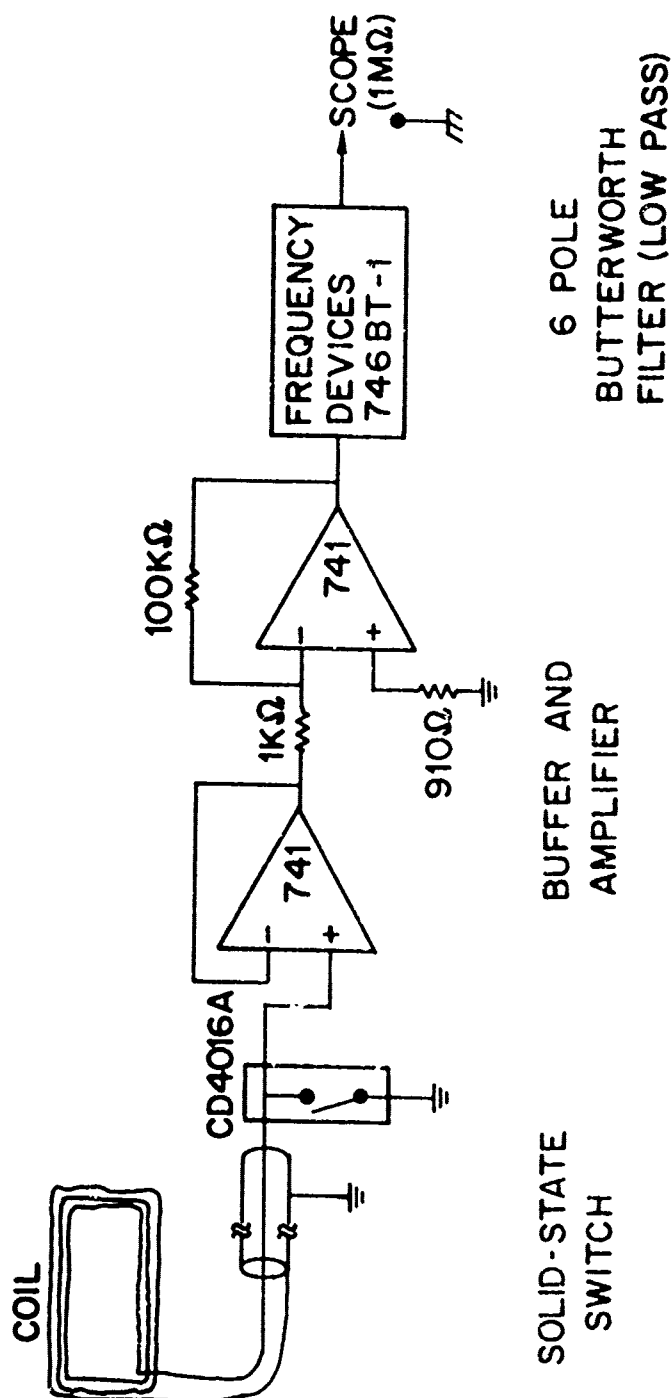
36

Fig. III.9 — Readout electronics for voltage induced in the pendulum pick up coil.

a thin 1000 Å polystyrene shield that stops ions but passes much of the incident plasma radiation through to the pendulum surface (more than 40% of the energy from 0.05-0.7 KeV and more than 95% of the energy from 0.7-50 KeV passes through to the pendulum surface[a]). Again, we noted no significant pendulum response during a shot.

Are six remote pendula adequate to measure ablation and target momentum?

A basic requirement of a momentum measuring array is that it confirm momentum conservation in the system being measured. Our array will not balance target-ablation plasma momentum if the pendula do not sample ablation plasma and target mass properly, or if the various pendula—all of which function in different immediate surroundings—are affected by phenomena other than material impact. To check this out, we irradiated a 12 μm CH foil attached to the target bearing pendulum that collects all the target mass and verified that the target momentum and the simultaneously measured blowoff momentum normal to the target

$$P_1 = 2\pi \int_0^{\pi/2} p(\theta) \cos\theta \sin\theta \, d\theta \qquad (III.8)$$

balance to within 30% (Fig. III.10). In Eq. (III.8) $p(\theta)$ is the momentum per steradian measured at an angle θ and cylindrical symmetry about the target normal is assumed. Similar balance between remotely measured ablation plasma and target-debris momenta for disk targets of varying diameter and thickness (0.3-1.2 mm, 5-40 μm) with varying absorbed irradiance and laser energy (5 × 10^{11} -- 3 × 10^{13} W/cm^2, 10 − 150 J) was also obtained, as shown in Fig. III.11.

(c.3) Choice of Target

In planar geometry experiments, where a finite diameter laser-spot irradiates a wide foil, care must be taken that events beyond the focal-spot periphery do not influence the experimental results too much. Such events, if significant, could not only complicate interpretation of the
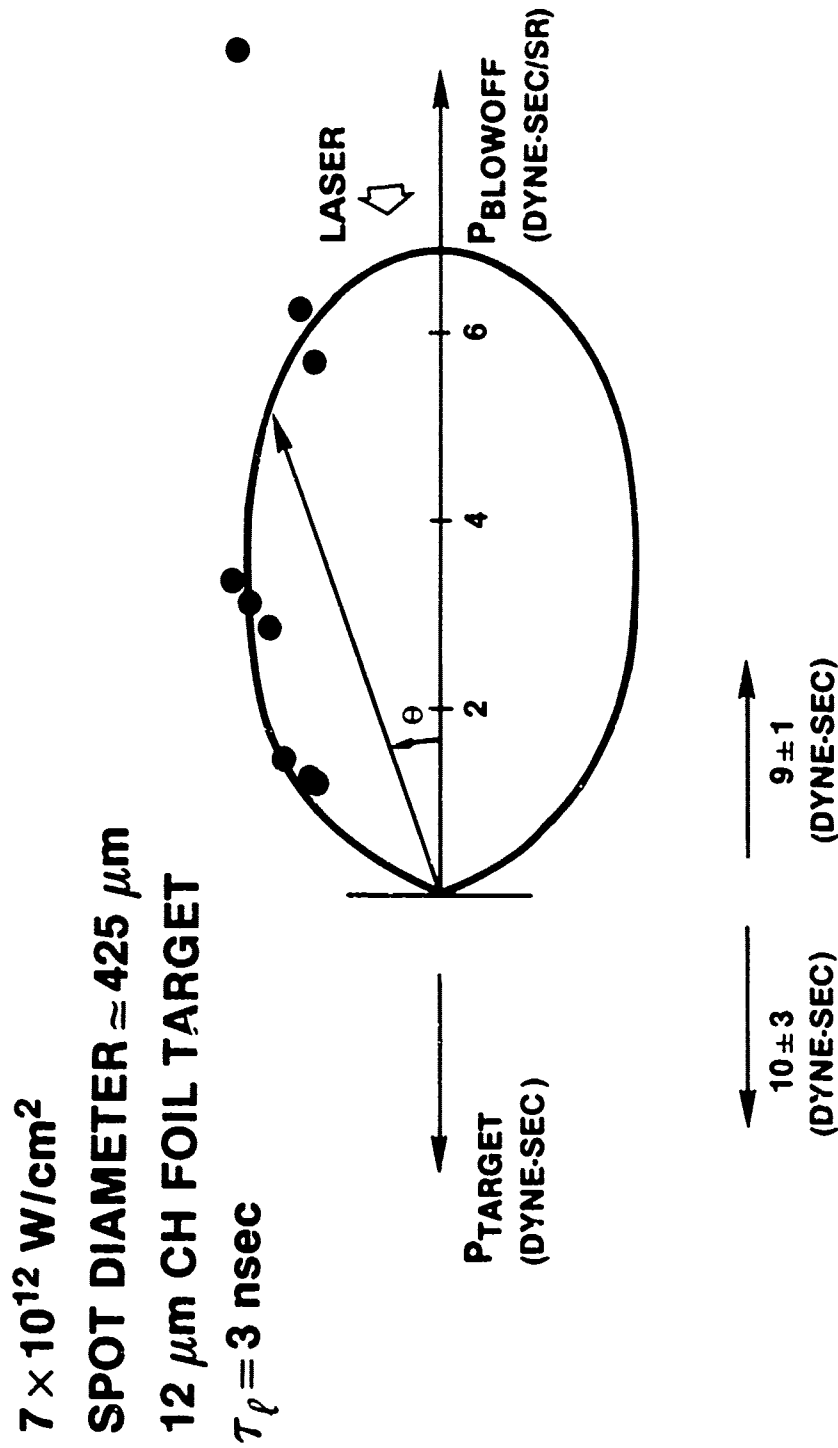
---

[a]Calculation by R.R. Whitlock

Fig. III.10 — Target momentum and remotely measured ablation momentum balance. The points in the figure are the results of three different shots.
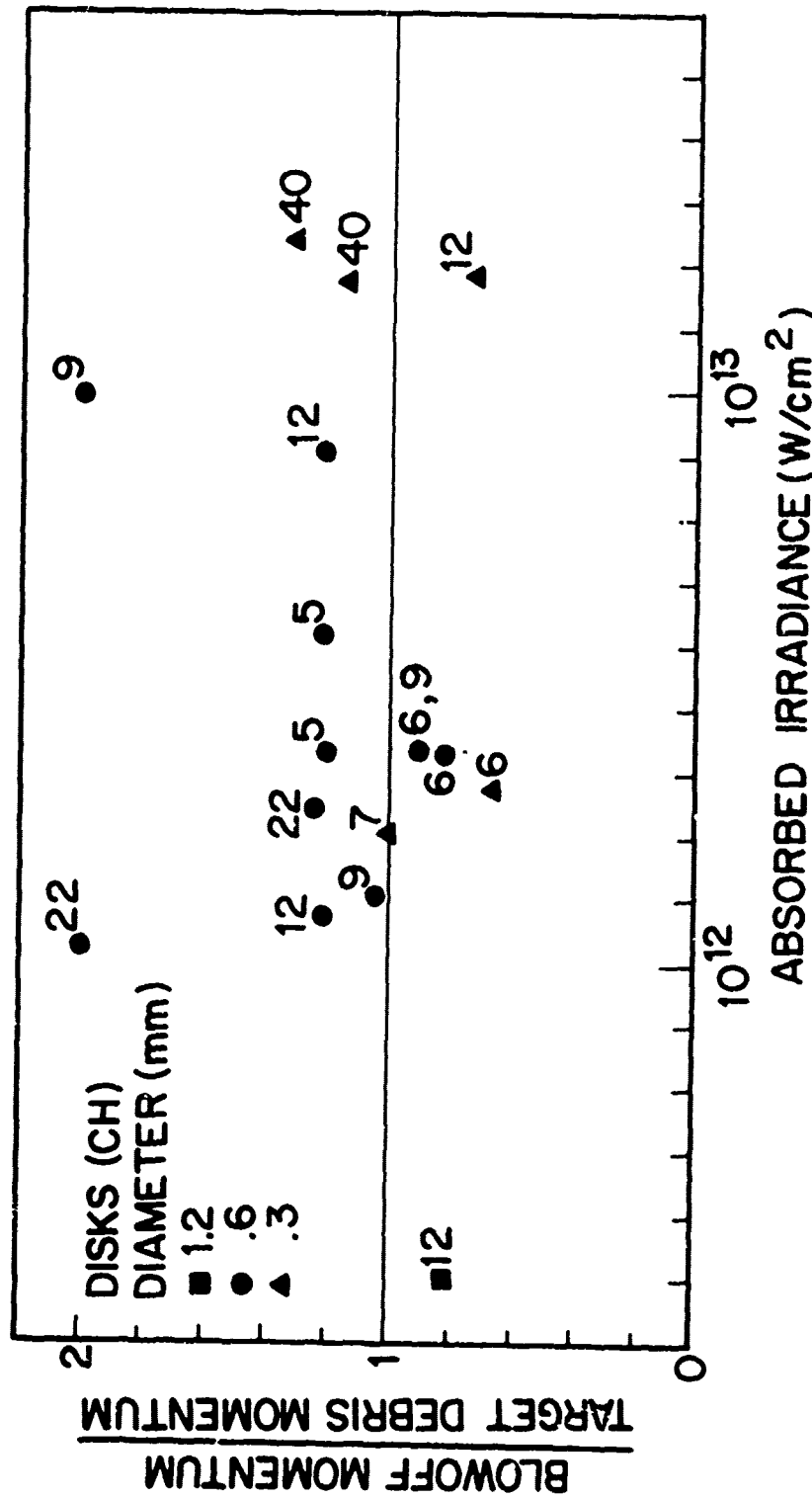
Fig. III.11 — Remotely measured ablation plasma and target-debris momenta balance. Momenta are calculated with Eq. III.8 in the text. Numbers near symbols refer to the disk thickness in microns.

results but could make them irrelevant to laser-fusion since a fusion pellet surface has no edges. Often the finiteness of the laser-spot is not a major problem since the phenomenon investigated requires high energies that exist only within the focal-spot (e.g., high energy x rays), or the diagnostic has time resolution, or the diagnostic has spatial resolution. But a pendulum has none of these features: It is time-integrating, has no spatial resolution, and a small amount of energy can easily heat a large amount of mass to produce a large momentum ($E = p^2/2m$). Small amounts of such extraneous energy may be provided by thermal conduction through the focal-spot periphery, by plasma flow along the target surface, or by radiation from the plasma plume. We note that a hole many times the size of the laser-spot remains in the target foil after a shot so that during or after the laser pulse a lot of mass was released. We also observe that liquid or solid target material has at times been accelerated over a distance of one meter—and can presently be found on the inner surface of our focusing lens. The situation is further complicated since the heating mechanisms may vary with laser-spot size or energy or laser irradiance. For example, thermal conduction that may not be significant at 10^{12} W/cm^2 will increase at 10^{14} W/cm^2 [$k \propto T^{5/2} \propto I$] and cause more momentum from beyond the focal-spot to be produced.

For these reasons we ordinarily use only disk targets with the pendulum diagnostic These disks have no significant mass outside their edges. Also, since their areas are well known, average irradiance and momentum per unit area may be reliably calculated.

The extent of the problem that may occur if wide foil targets and ballistic pendula are used together is shown by the following experiment: We measured the target debris and plasma blowoff momenta (with the pendulum array) of 30 μm thick CH foils as a function of laser-spot size which was varied by aperturing the incident laser beam. The irradiance was 1×10^{12} W/cm^2 and the momenta were calculated using equation III.8 As Fig. III.12 shows, the ratio
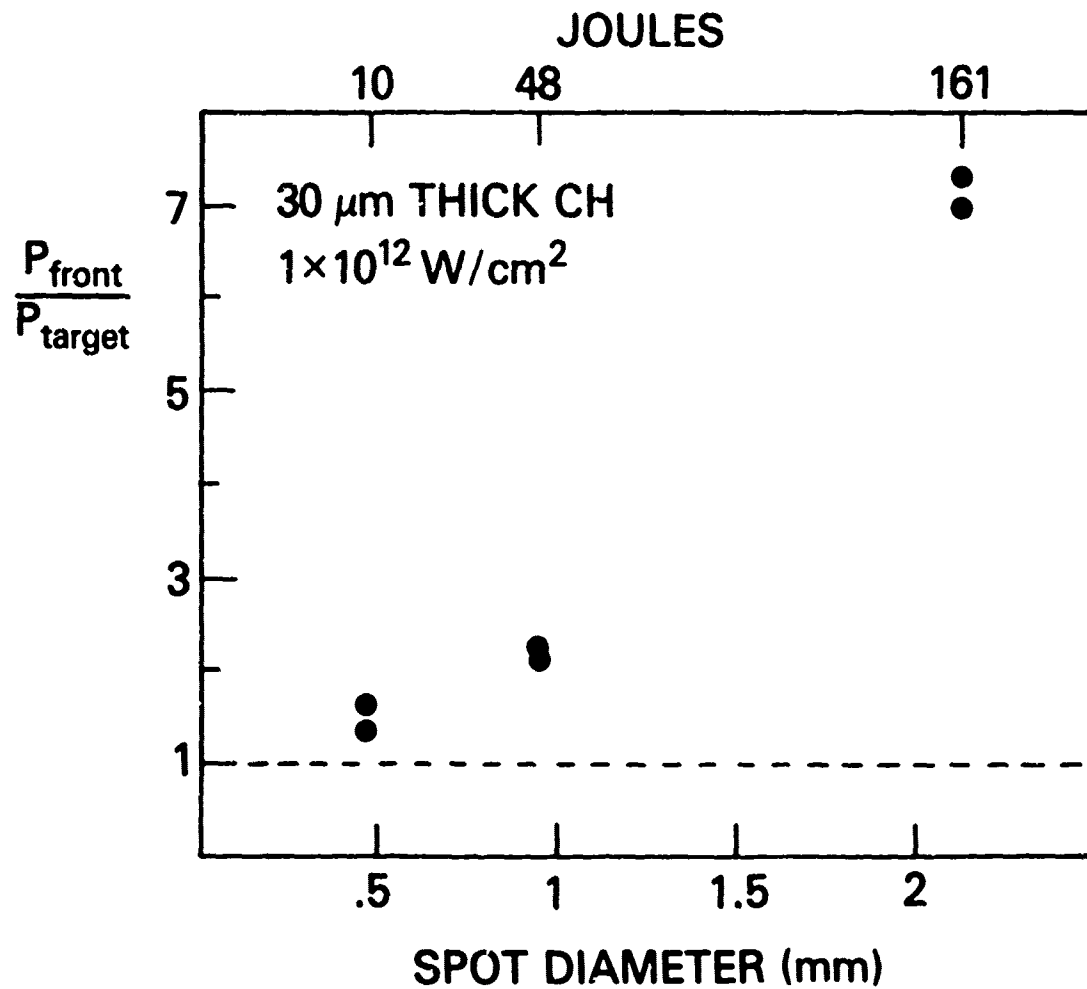
Fig. III.12 — Ratio of blowoff to target-debris momenta at 1×10^{12} W/cm^2 as a function of laser spot size. Momenta are measured with the remote pendulum array

of blowoff to target-debris momentum does not stay constant but increases dramatically with laser-spot size. An examination of the momentum per unit focal-spot area (90% energy content) shows that the variation in Fig. III.12 is due to a corresponding variation in the blowoff momentum; the target debris momentum per unit laser-spot area does not vary by more than ±25%, a scatter consistent with shot-to-shot variation and uncertainty in the laser-target interaction area as the spot size is changed. These results are explainable if an energy source whose effect increases with spot size (plasma plume radiation for example?) heats a lot of surface material that is sensed by the blowoff pendula, but does not create sufficient pressure to accelerate foil material outside the focal spot (Fig. III.13). To avoid such complications we use disk targets with the pendulum diagnostic.
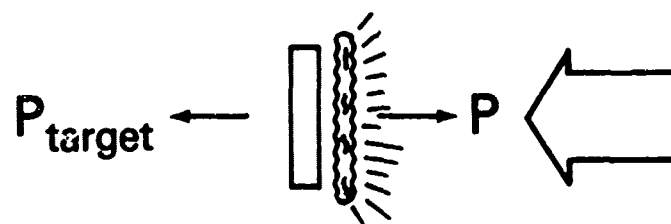
(c.4) Absolute Calibration

The nature of the plasma-pendulum collision (elastic?, inelastic?) and sputtering from the pendulum surface affect its in-situ calibration. To account for these effects, the momentum of ions reflected or sputtered from a pendulum surface is measured and the bench calibration (Eq. III.7) appropriately adjusted. A mass accounting technique and a comparison of pendulum measurements to those of other diagnostics verify the calibration.

The double pendulum, sketched in Fig. III.14, consists of two pendula enclosed in an aluminum shield containing a small hole. Plasma enters through the shield's hole striking the pendulum surface being calibrated. Any material reflected or sputtered from this surface is detected by a second pendulum built in the shape of a rectangular cavity." We assume that no subsequent reflection or sputtering takes place, or that particles reflected or sputtered off one part of the cavity surface eventually deposit their momentum within another part of the cavity. Consequently, we write:

---

*This mylar cavity has the dimensions (width × height × depth) 5.4 × 2.2 × 1.6 cm and has two 1.0 × 1.0 cm plasma entry holes. The surface being calibrated is bent 10°-15° to the vertical axis so that ions reflecting in a mirror-like fashion do not escape back through the hole.

DISK TARGET

$$P_{target} \longleftarrow \quad \longrightarrow P$$

FOIL TARGET

$$P_{target} \longleftarrow$$

$$\longrightarrow P_{side}$$

$$\longrightarrow P$$

$$\longrightarrow P_{side}$$
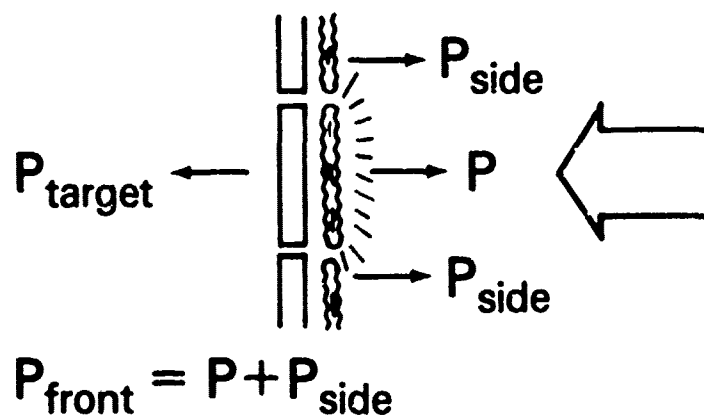
$$P_{front} = P + P_{side}$$

Fig. III.13 — Model that may explain the results of Fig. III.11. Extra blowoff momentum seen by ballistic pendula comes from regions beyond the focal-spot.

PENDULUM ① DETECTS PLASMA

PENDULUM ② DETECTS REFLECTED PLASMA OR SPUTTERED MATERIAL
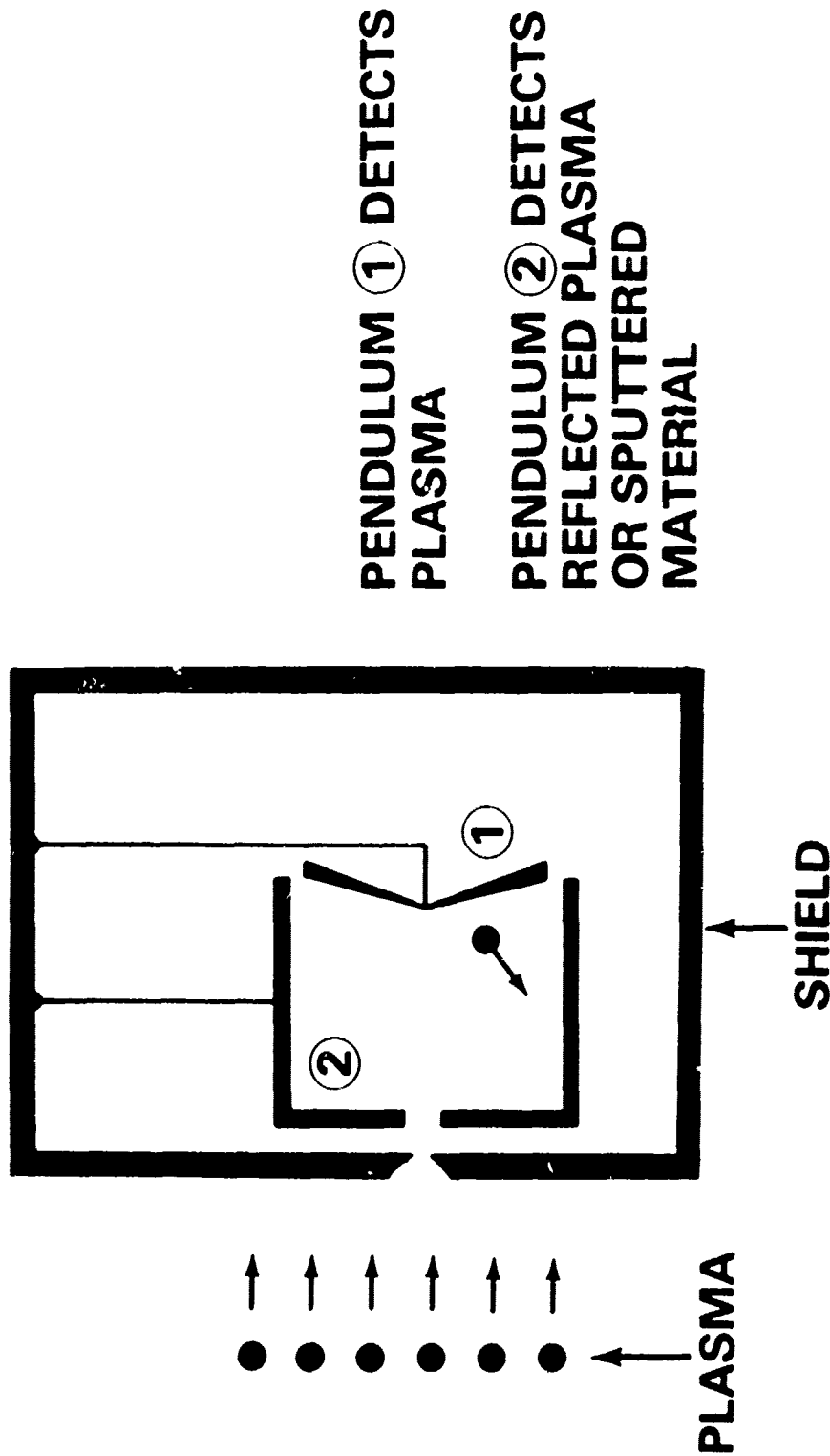
SHIELD

PLASMA

Fig. III.14 — Schematic of our double-pendulum. Pendulum (1) measures momentum of incoming plasma. Pendulum (2) measures momentum of material reflected or sputtered from pendulum (1).

$$p_1 = p + \gamma p \equiv \beta p \tag{III.9}$$

$$p_2 = \gamma p \tag{III.10}$$

where p is the momentum of the plasma, p_1 is the momen·· of the pendulum being calibrated, γp is the momentum of sputtered or reflected material and p_2 is the momentum deposited in the cavity of the second pendulum. The quantity β is a calibration factor relating pendulum momentum (using bench calibration) to the momentum of the incoming plasma. It is given by

$$\beta = [1 - p_2/p_1]^{-1} \tag{III.11}$$

The value of β was determined for both brass and mylar surfaces to be 2.4 ± 0.6 (Table III.1).[a]

To verify this calibration we compare the mass of a disk target to the mass calcu ted from remote measurements of ablation plasma and target-debris energies and mom· using

$$\text{disk mass} = 2\pi \int_0^\pi \frac{p^2(\theta)}{2 E(\theta)} \sin \theta \, d\theta. \tag{III.12}$$

The results (Table III.1) show that we account for the disk target mass to much better than a factor of two. Had we not calibrated the pendulum in-situ the calculated mass would have been six times larger. A comparison of the ablation plasma momentum measured with pendula and inferred from energy and velocity measurements $[p(\theta) \equiv 2E(\theta)/\bar{u}(\theta)]$ using Eq. III.8 at irradiances between 4×10^{11} a: ! 4×10^{13} W/cm^2 is also shown in Table III.1. The two agree to about 10%.

---

[a] Brass and mylar surfaces were used in our experiments for historical reasons In retrospect mylar is the better surface since data on the sputter off its surface shows less scatter than data on the sputter off a brass surface

Table III.1. Data used to determine and confirm the pendulum calibration. Top row: Calibration coefficient β inferred from double pendulum measurements. Middle row: Ratios of mass inferred from pendula to disk target mass. Bottom row: Ratios of momentum measured with pendulum array to momentum inferred from calorimeter (energy) and ion-collector (velocity) measurements.

	Raw Data	The Mean and the Standard Deviation
Calibration Coefficient β	1.3, 1.4, 1.8, 2.0, 2.1, 2.5, 2.6, 2.7, 2.8, 2.9, 3.2, 3.5	2.4 ± 0.6
$\dfrac{\text{Inferred Mass}}{\text{Disk Mass}}$	0.5, 0.5, 0.6, 0.9, 1.1, 1.2, 1.4, 2.0	1.0 ± 0.5
$\dfrac{\text{Momentum from Pendula}}{\text{Momentum from cals. and ion collectors}}$	0.8, 0.9, 0.9, 0.9, 1.0, 1.2, 1.2, 1.4, 1.5	1.1 ± 0.2

D. Double Foil Technique[a]

Final target velocities must be accurately measured so that the viability of the hollow pellet concept may be tested. Previous studies of planar target motion involved asymptotic measurements that inferred target velocity from the velocity of its debris, but could not diagnose the target directly; and optical methods that could not distinguish between the high density bulk of the target and the lower density plasma that may preceed and obscure it.[6] The double-foil technique permits time resolved diagnosis of the high density part of the accelerated target. The technique consists of placing a thin foil (impact foil) some distance behind the laser-accelerated target. Upon collision with the laser-accelerated target the impact foil responds and the behaviour of the target is inferred from this response (Fig. III.15).

The choice of the target and impact foil material, their dimensions, and the spacings between the two foils depend on what is being studied. Generally, the impact foil should be thin enough so that the shock-transit-time from its front to rear surfaces is shorter than any other resolvable time scale of interest. Examples of such time scales are the time-of-flight of the target to the impact foil, or the time scale over which the double foil collision takes place (~ target thickness/target velocity). If the shock-transit-time is short, it may be ignored, and the target behaviour at the front surface of the impact foil directly related to the response at the rear of the impact foil. If, in addition, we choose the areal density of the impact foil to be much greater than that of the target we may be able to time resolve its recoil and, using simple Newtonian mechanics or a fluid code, determine the target impulse and density profiles (A high areal density is required so that the accretion of target mass on the impact foil's surface is negligible.) Unfortunately, we have determined (Section IV) that the recoil of the impact foil is obscured by low pressure (and probably low density) material ejected from its rear surface after the collision so that x-ray backlighting (not yet available in our laboratory) may be required to
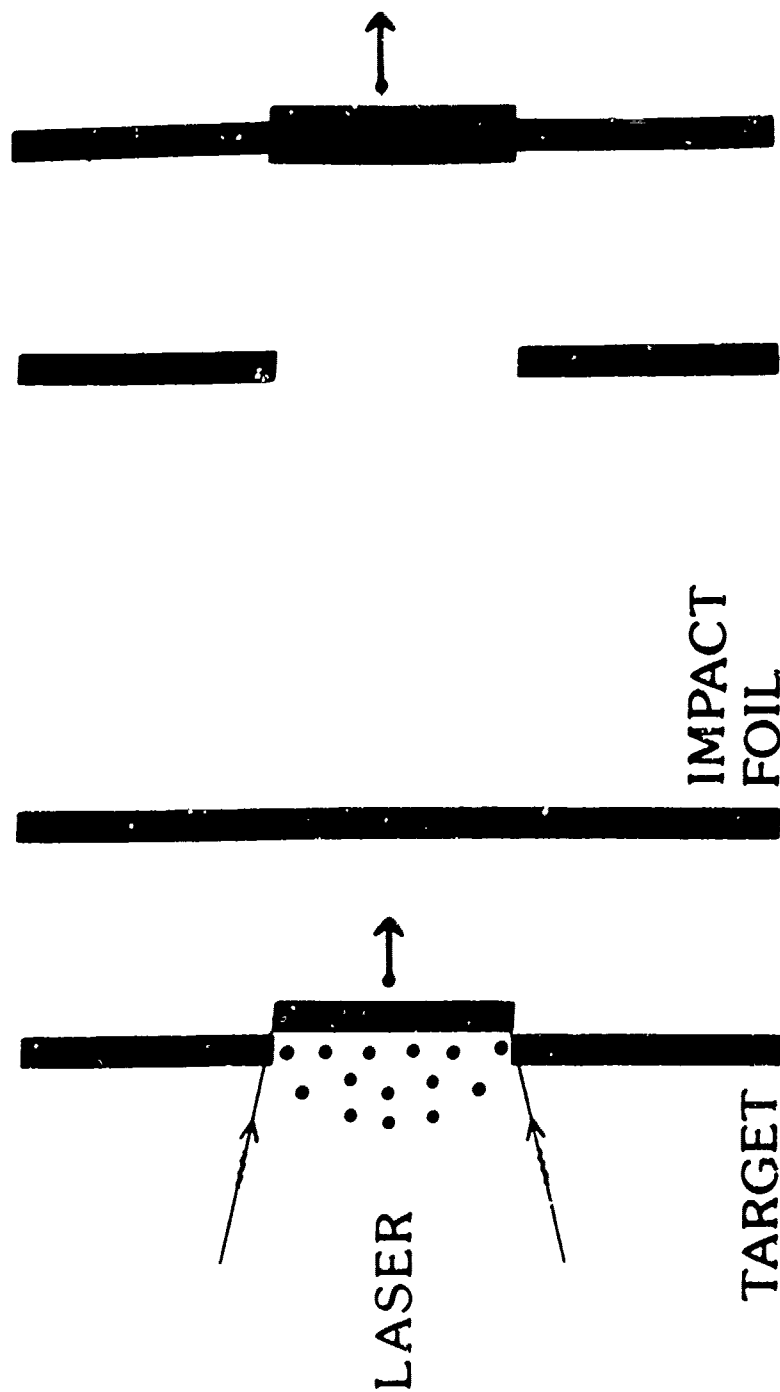
Fig. III.15 — Schematic of the double-foil concept. Behaviour of the laser accelerated target is referred from the response of the impact foil to the collision

IMPACT FOIL

TARGET

LASER

do this experiment.[a] Meanwhile, the response of the impact foil to its collision with the target is being used to measure the velocity of the dense target (Section IV), and to study the effects of nonuniform irradiance,[8] nonuniform target density, nonuniform target thickness, or target ripple[25] on the uniformity of the acceleration. For most of the target velocity measurements reported here the target was a 7 or 10 μm thick polystyrene foil and the impact foil was 7 μm aluminium. Spacing between the foils was typically 200-700 μm. Details of the target-impact foil collision are described in Section IV.

The experimental setup is shown in Fig. III.16. Shadows of the target and impact foil are viewed in two ways: A two-dimensional image is frozen in time by a short (< 0.5 nsec) 5270 Å probe pulse[6] synchronized with respect to the main laser,[b] or a one-dimensional but continuous (in time) image is obtained with a streak camera (Hadland Imacon 675 with an S-1 tube). In the latter case illumination is provided by a long duration (~ 10 nsec) laser probe made by frequency doubling and stacking a small portion of the main laser pulse. Time markers cut into the probe by a fast pockels cell provide a convenient time calibration.

---

[a] We note that the use of the double-foil technique to model multishelled pellets, to study velocity multiplication, and similar experiments, is also of great interest.
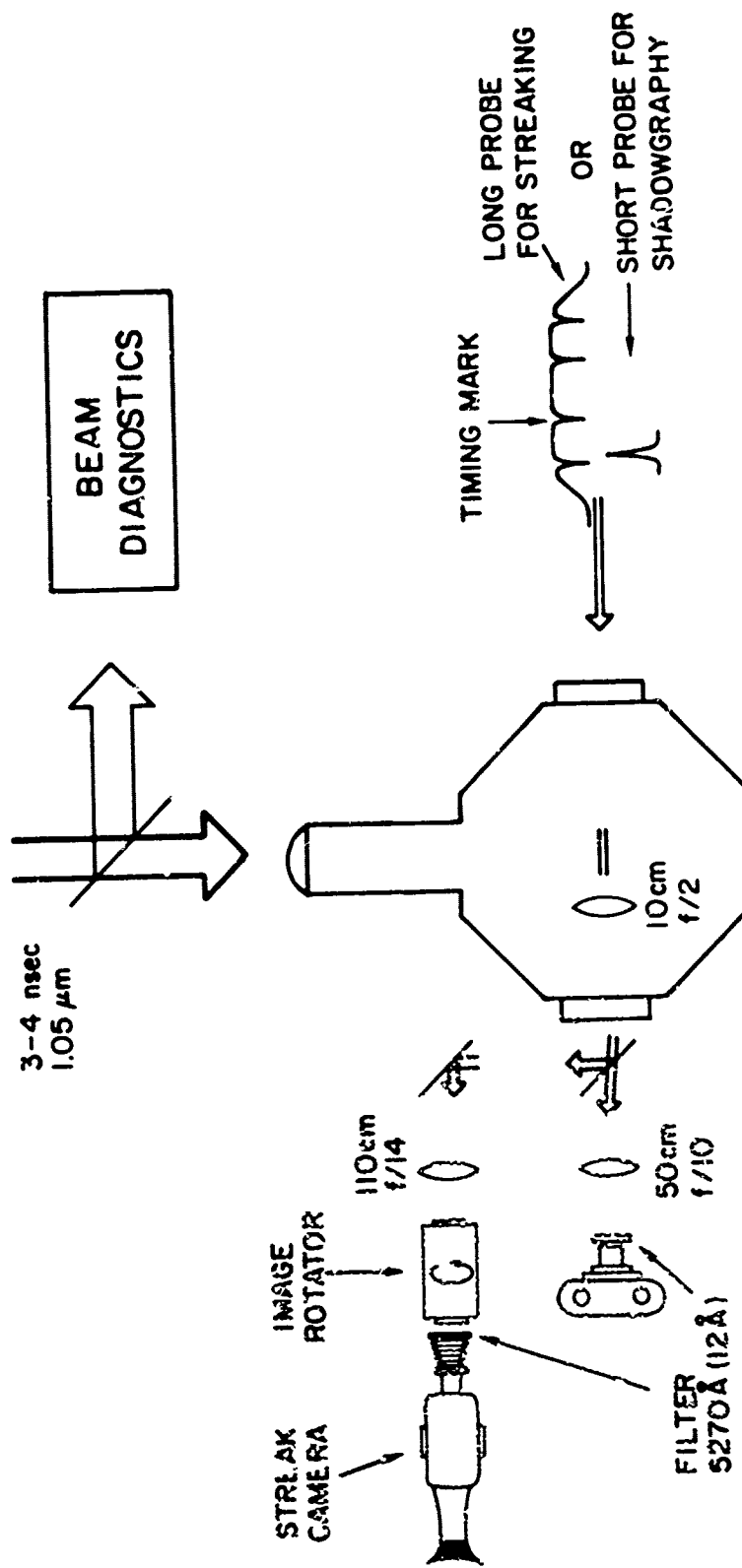[b] Shadowgraphy was set up by J A Stamper

Fig. III.16 — Experimental arrangement for the double-foil experiments.

Section IV

EXPERIMENTAL RESULTS

In this section the momentum, energy, and velocity characteristics of plasma ablating from planar targets irradiated by long (4 nsec FWHM, $< 10^{14}$ W/cm^2) Nd-laser pulses are measured. The dependence of ablation parameters such as ablation pressure, ablation velocity, and mass ablation depth (or mass ablation rate) upon absorbed irradiance is determined and compared to existing theory. Large laser spots are used in these experiments so that the results are not sensitive to boundary affects. Velocity of the dense accelerated target is measured with a novel double-foil technique and compared to predictions made from the ablation parameters and a simple rocket model. Dense target velocities larger than 100 Km/sec have been observed.

A. Angular Distribution of Ablation Plasma

Angular distributions of the ablation plasma energy $E(\theta)$, momentum $p(\theta)$, and velocity $\bar{u}(\theta)$ for an irradiated disk target are shown in Fig IV.1; $\bar{u}$ is a mean velocity unfolded from ion-collector traces as explained in Section III. All detectors are in the horizontal plane and cylindrical symmetry about the target normal is assumed. Angular distributions from various disk (0.3 to 1.2 mm diameter) and wide foil targets have similar shapes. The angular distribution of the blowoff momentum, for example, may be characterized by a half-cone angle $\cos^{-1}(P_1/P) = 40°$ for both the disk and wide foil cases; $P_\perp$ is the normal component of the total momentum P obtained by integrating $p(\theta)$ over all solid angles. We use such angular distributions to determine the magnitudes and scaling with irradiance of the ablation parameters. Although any two
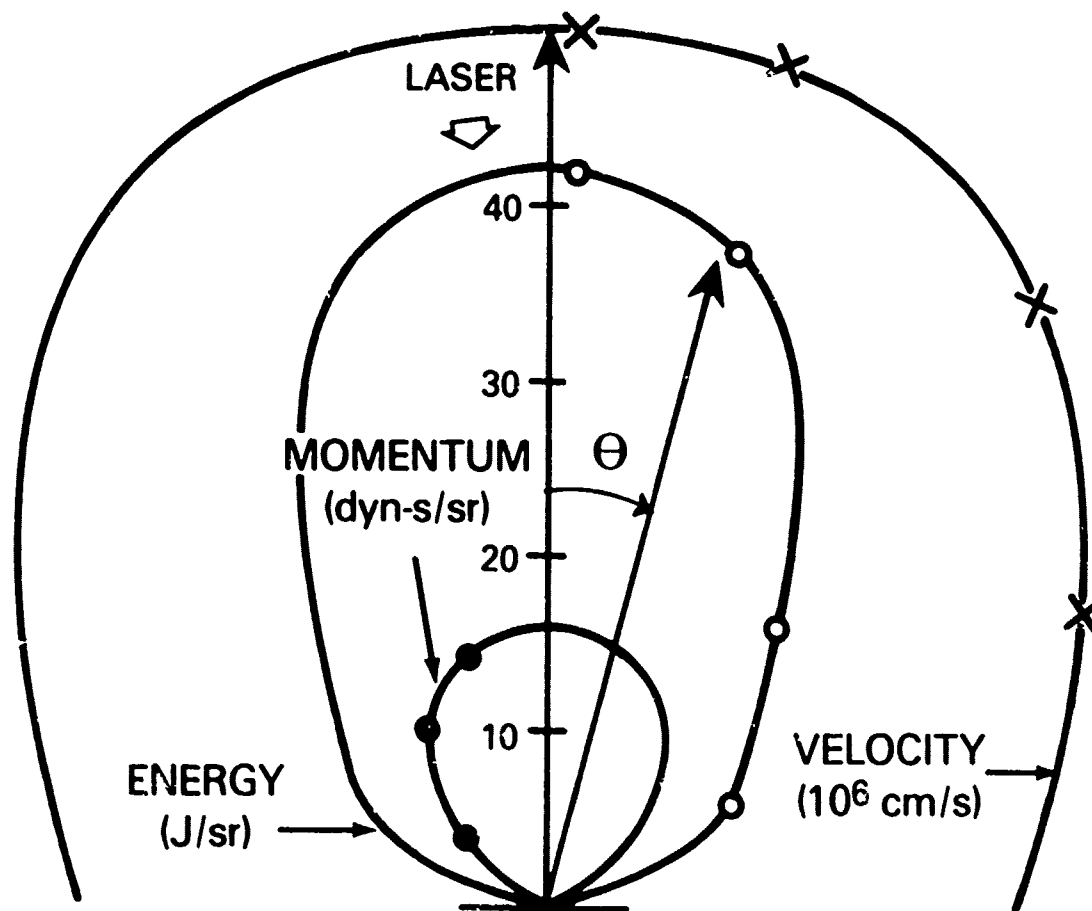
52

Fig. IV.1. Distribution of blowoff velocity, energy, and momentum measured with time-of-flight ion collectors, plasma calorimeters, and ballistic pendula respectively. The target is a 1.2 mm diameter CH disk irradiated at 3×10^{12} W/cm^2.

of the measured quantities would have been sufficient, we measure all three with independent diagnostics to verify the self consistency of our results.

To examine the nature of plasma flow from the target surface we irradiated a polystyrene target onto which we evaporated two small aluminum dots ($260\ \mu$m diameter, $2\ \mu$m thick) as sketched in Fig. IV.2. An x-ray pinhole camera ($>$ 1 KeV) viewed the target and dots edge-on.[a] We assume that plasma from the slightly raised aluminum dots follows the same flow pattern as plasma from the rest of the target. Since aluminum is a much stronger x-ray emitter than CH in the sensitive range of the pinhole camera, the emission for the aluminum dots acts as a tracer for the overall plasma flow.

The results, shown in Fig. IV.3, are reminiscent of a fluid flow pattern near the surface of a disk. In particular, the flow direction, and therefore the blowoff angular distributions in Fig. IV.1 appear to be largely determined near the target surface. This is consistent with the above observation that the angular distributions of ablation parameters for targets irradiated by various spot sizes are similiar. Fig. IV.3 also suggests that ablation plasma from a region of the target surface maps into a distinct solid angle. Consequently, small detectors, many centimeters from the target surface, sample plasma that originated from different regions of the target.[b] Therefore, when calculating plasma parameters characteristic of an entire target irradiated by a spatialy nonuniform laser beam, such as average pressure on a target surface, the entire plasma angular distribution should be taken into account.

B. Measurement of Ablation Parameters

Scaling of ablation pressure with absorbed irradiance[1] $\mathscr{P} \propto I_a^{0.8}$ is shown in Fig. IV.4. The pressure is deduced from $\mathscr{P} = P_1/\tau A$ where τ is the FWHM laser pulse duration (4 nsec)

---

[a] Measurement by M.J. Herbst For a fuller description see M J Herbst and J Grun. NRL Memo 4436, 1980, submitted for publication

[b] When the plasma becomes collissionless thermal expansion will modify this simple picture However, the ratio of ion thermal to directed velocity is small so that the modification is small
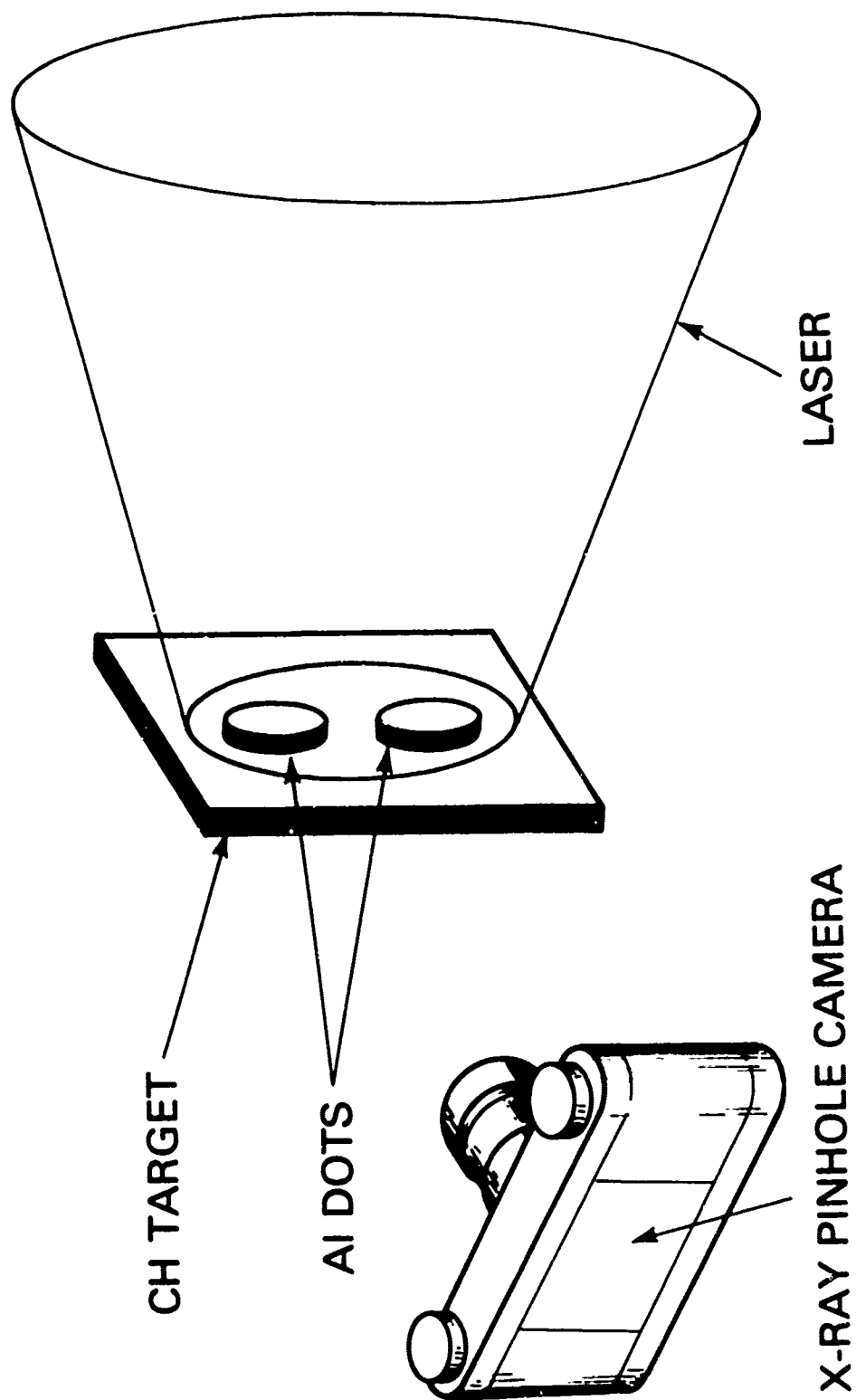
LASER

CH TARGET

Al DOTS

X-RAY PINHOLE CAMERA

Fig. IV.2. Experimental setup to observe plasma flow near target surface.

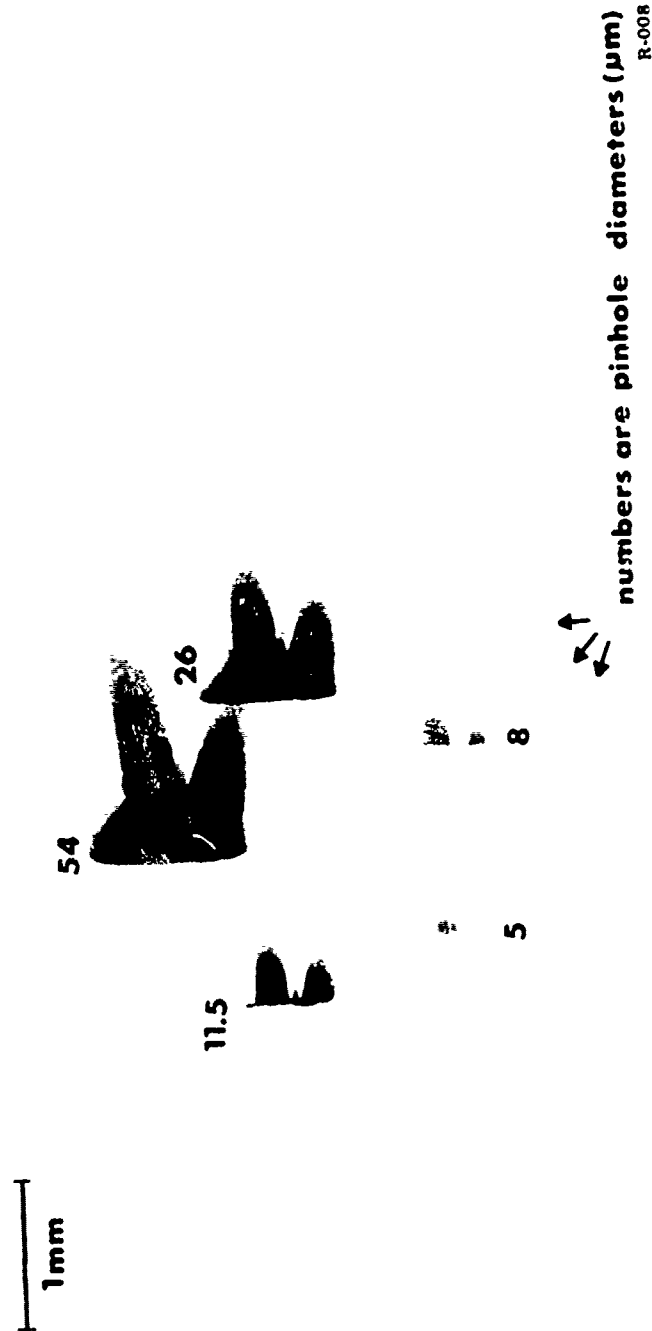**numbers are pinhole diameters (μm)**

R-008

Fig. IV.3 Edge-on x-ray pinhole photograph of an irradiated CH target with two aluminum dots on its front surface (see Fig. 2). Each image is labeled with the diameter of the pinhole through which it was photographed. The x-rays photographed have energies greater than 1 keV (14.1 μm thick Be filter is used). Dots are 260 μm in diameter and 2 μm thick.
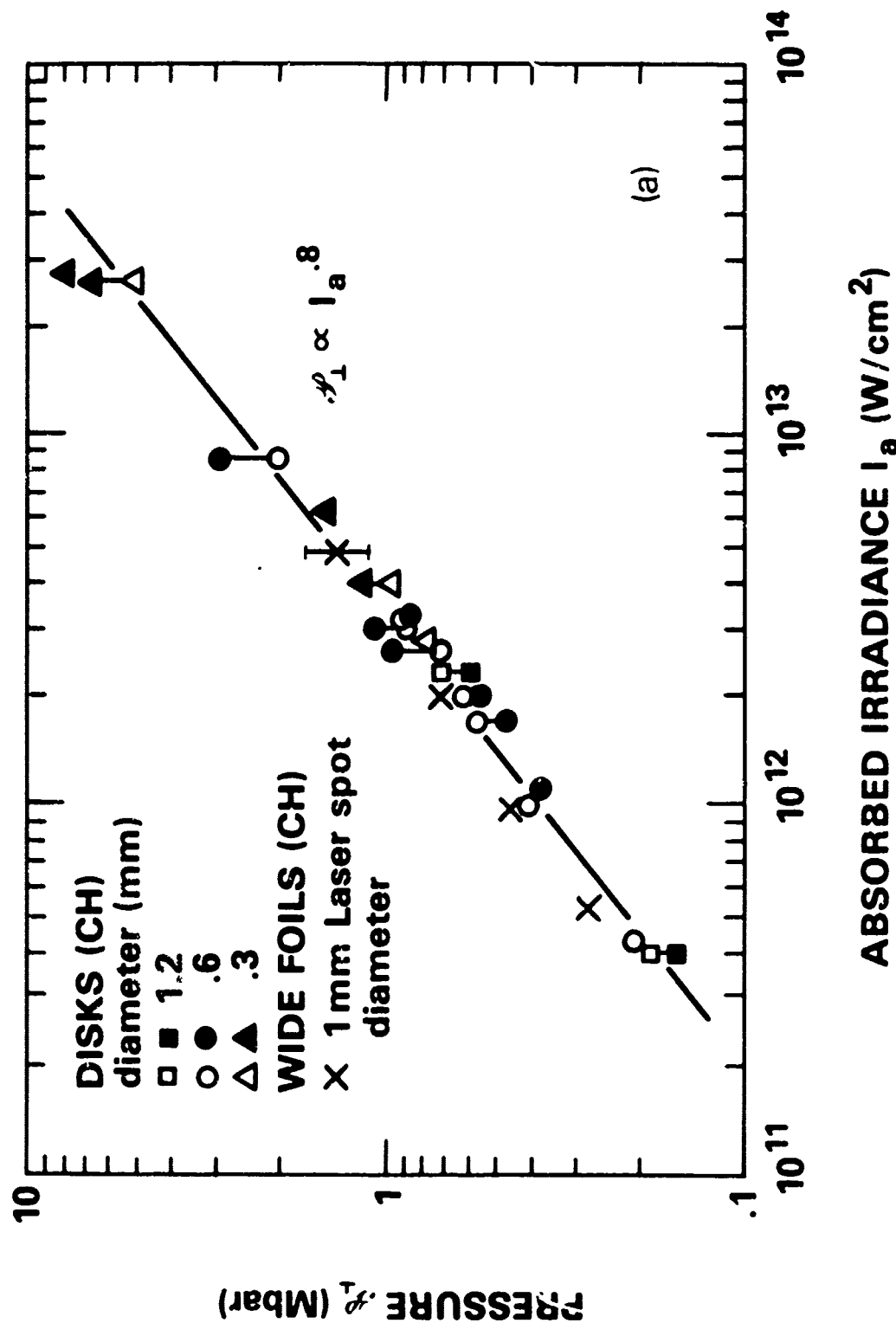
1mm

Fig. IV.4. Ablation pressure versus absorbed laser irradiance for disks and wide foil targets. The data denoted by ■, ▲, ● are inferred using momenta measured with ballistic pendula. The data □, △, ○ are obtained using calorimeter and time-of-flight measurements.

and A is the area of disk targets or laser-spot area on wide foil targets. The momentum from disk targets (defined in Eq. III.8) was measured in two independent ways: first, using the pendulum array (dark markers); second, using energy and velocity data (open markers); wide foil results (X) used the latter method only. Agreement between both methods increases our confidence in the measurements.

We verified that the pressure in Fig. IV.4 inferred from asymptotic measurements, is the same (within 30%) as the ablation pressure calculated from measurements of the target acceleration[a].

The aspect ratio $R/\Delta R$ necessary to accelerate pellet shells to 200 km/sec may be roughly estimated for a given pressure from the one-dimensional rocket equations:

$$\mathscr{P} = \frac{d}{A} \frac{m v}{dt} \approx \rho \Delta R \, v/\tau \tag{IV.1}$$

$$R \approx v\tau \tag{IV.2}$$

which give

$$\frac{R}{\Delta R} \approx \rho v^2 / \mathscr{P}_1 \approx 400 \rho_{gm/cm} / \mathscr{P}_{1 Mbar} \tag{IV.3}$$

where $m, \rho, v, \Delta R, R$ are the shell mass, density, velocity, thickness, and radius; and a small ablation depth is assumed. Thus, higher pressure (irradiance) or lower shell density reduce the pellet aspect ratio. For example, at 5×10^{13} W/cm^2, where the pressure is ~ 10 Mbar, $R/\Delta R$ $\sim 40 \rho$ which is an aspect ratio of 40 for plastic shells, or less for lower density shells made of lithium or deuterium.

There is also latitude in choosing an irradiance to minimize pellet aspect ratio while retaining good hydrodynamic efficiency in the pellet design. To see this we note that ablation velocity u_1 and mass ablation depth $d = m_a/\rho A$ ($\dot{m}_a \approx \rho A d/\tau$) vary as the 0.2 and 0.6 power

---

[a] Target acceleration $\equiv$ target velocity/τ Target velocity is measured in Part D

58

of the absorbed irradiance (Fig. IV.5). Here $\dot{m}_a$ is mass ablation rate. From these scalings, and the one dimensional rocket equations,

$$\frac{v}{u_1} = \ln\left(\frac{m_o}{m}\right) \approx \frac{d}{d_a} \tag{IV 4}$$

$$\eta_h = \frac{(v/u_1)^2}{e^{(v/u_1)} - 1} \approx \frac{v}{u_1} . \tag{IV.5}$$

where m_o is the initial target (rocket) mass, it can be shown that the initial thickness of a target accelerated to a given velocity for a constant pulse duration, varies as $d_o \propto I_a^{0.8}$; whereas the hydrodynamic efficiency varies weakly as $\eta_h \propto I_a^{-0.2}$. Consequently, increasing target thickness and irradiance to lower the aspect ratio and increase the smoothing of irradiance nonuniformities[2] causes only small changes in hydrodynamic efficiency.

These ablation results are in basic agreement with planar[3-7] and spherical geometry[8,9] theories (shown in Table IV.1), though agreement with Jarboe's et al. theory[7] that fixes the sonic plasma exhaust at critical density is not that good. Theories assuming inhibited thermal transport[10] in the region between the ablation and critical surfaces are not in very good agreement with experiment. Consequently, it appears that basic conservation laws without any ad-hoc thermal transport inhibition control the laser-plasma interaction in this irradiance and pulse-length regime.

C. Laser Spot-Size and Target-Diameter Effects

Studies on flat targets are subject to the criticism that phenomena at the focal-spot periphery may distort effects ascribed to the spot as a whole. Such finite laser-spot effects may include self-generated magnetic fields[11] or energy leakage laterally across the focal-spot edge. Moreover, extraneous plasma from areas outside the focal-spot may also contribute to the observed results. To check for these effects we placed planar targets in the near-field of the
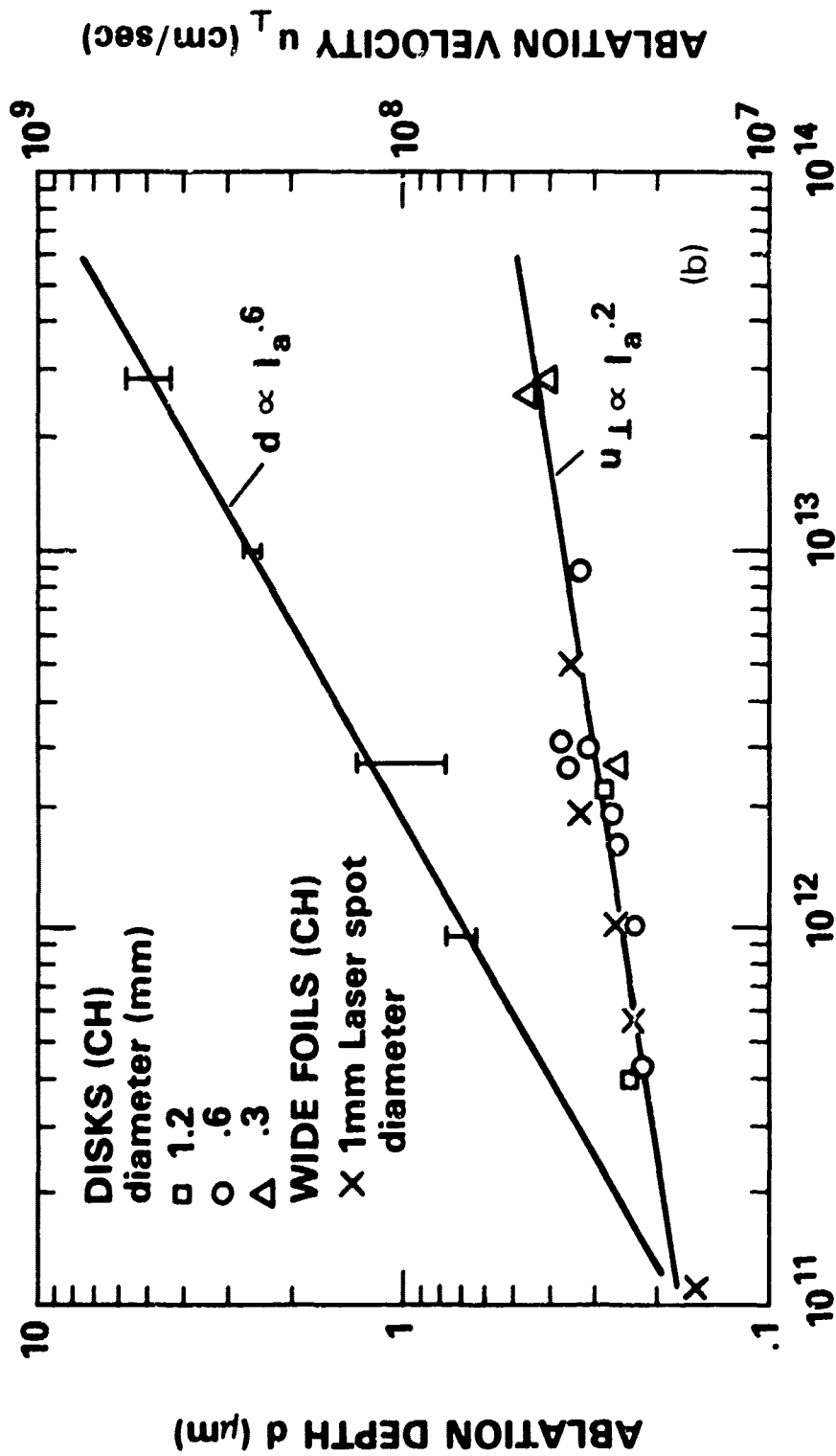
Fig. IV.5. Ablation depth d and normal ablation velocity u_t versus absorbed irradiance I_a. Points are obtained using calorimeters and time-of-flight detectors.

Table IV.1 Summary of theories discussed in Section II
and Table II.1. Table entries are the exponents in
$\alpha \equiv I_a^n$ where α is an ablation parameter. Theories
referred to are found in references 3-10.

THEORY	$\mathscr{P}_\perp$	$u_\perp$	d or $\dot{m}$
KIDDER	.75	.25	.50
CARUSO	.75	.25	.50
AHLBORN	.78*	.22*	.56*
JARBOE	.66**	.33**	.33**
PUELL	.78	.22	.56
NEMCHINOV	.78	.22	.56
GITOMER			.56
MAX	.57	.09	.48
EXPERIMENT	0.8	0.2	0.6

$*\eta^{\pm 1/q}$, $\eta^{2/q}$ IN AHLBORN'S EXPRESSIONS HAVE
HERE BEEN TREATED AS CONSTANTS. η IS THE
ABSORPTION FRACTION.

**JARBOE ET AL. DERIVE EXPLICITLY A RELA-
TION FOR u_1 ONLY. TO GET THE OTHER TWO
QUANTITIES WE USED THE RELATIONS
$\mathscr{P}_\perp \propto n_c u_1^2$ AND $\dot{m} \propto n_c u_1$ IMPLIED BY HIS
THEORY; n_c IS THE CRITICAL DENSITY

focusing lens and varied the spot-size by aperturing the laser beam while monitoring the abla-
tion velocity. Because of laser energy limitations, this experiment used an average irradiance of
1×10^{12} W/cm². But even at this low irradiance the velocity did vary with spot-size[a] (Fig.
IV.6). Notice, however, that velocity changes were small if the laser spot diameter was
sufficiently large (≥ 1 mm).

Both the spatial profile of the incident irradiance and the fraction of energy escaping
through the focal spot periphery change with varying spotsize. Since the number of ions at a
particular velocity depends on absorbed irradiance, these phenomena could contribute to the
velocity variation in Fig. IV.6a. Lateral heat flow especially could shift energy from a higher to
a lower portion of the effective irradiance profile and increase the fraction of low velocity ions.
Large spot-size experiment, with relatively uniform illumination, have a smaller fraction of
absorbed energy escaping through their edges and, therefore, behave independently of spot-size
diameter.

Stationary ablation should produce highly peaked ion velocity distributions.[12-14] In most
of our cases the ion velocity distributions are highly peaked with a peak velocity to FWHM
ratio of 3:1. However, under some experimental conditions even narrower distributions (peak
velocity: FWHM = 7:1) and broader distributions (peak velocity: FWHM = 2:1) are observed.
These are shown in Fig. IV.6b,c. We note that generally disk targets produce narrower traces
then foil targets, small laser spots produce narrower traces than large laser spots, and small
diameter disks produce narrower traces than large diameter disks. Also, the spread of the most
highly peaked cases is consistent with that expected from temporal variation of the laser beam
alone.[b] However, various experiments that attempted to identify the cause of the ion trace
broadening proved inconclusive

---

[a]Measurement by R Decoste
[b]We assume that the time averaged scalings in part B apply at each point in time as well We then obtain $dN \propto I^{0.6}(t)dt$
and $u \propto I^{0.2}(t)$ where I, N, u, t and the irradiance, number of ions, ion velocity and time respectively
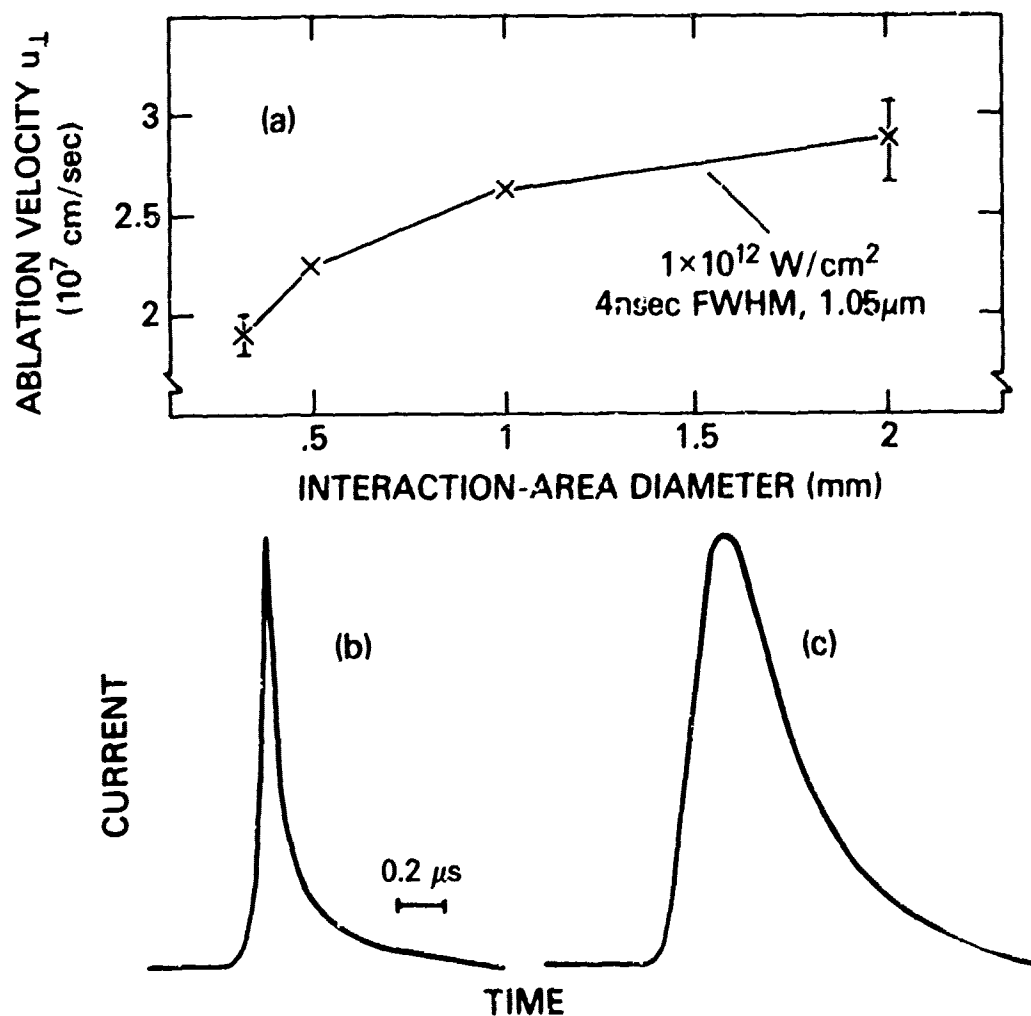
Fig. IV.6.(a). Ablation velocity $u_\perp$ vs interaction-area diameter for wide foil targets. (Interaction-area is defined as the area containing 90% of the incident laser energy.)

$$u_\perp \equiv \left[\int_0^{\pi/2} \left[\frac{2E}{\bar{u}^2} \right] \bar{u} \cos\theta \sin\theta \, d\theta \right] \Bigg/ \int_0^{\pi/2} \left[\frac{2E}{\bar{u}^2} \right] \sin\theta \, d\theta$$

(b), (c). Examples of narrow and broad ion collector traces. The collectors are 28 cm from the target and at an angle of 2° to its normal.

Accordingly, to get results representative of large systems, our experiments with foil targets are done using 1-mm diameter laser spots. Uniformly irradiated[a] disk targets are also used in some cases. These disks have two advantages over foil targets; first they provide an unambiguous interaction area to use in calculating irradiance and ablation pressures or mass ablation depths; second, any laser energy that escapes the interaction area is easily measured and the effect on ablation parameters is easily estimated. A small amount of energy, in fact, does escape from the front (laser side) to the rear of disk targets. This is shown in Fig. IV.7 where the energy measured at target rear and the expected target kinetic energy (from a one-dimensional rocket model) are compared. For small diameter disks (300-600 μm) less than 20% of the absorbed energy flows to the target rear whereas for large diameter disks (1 mm) this amount is only 5%. Such small energy loss out the target edge has minimal effects on the measurement of ablation parameters.

At the irradiances employed here, this lost energy is probably due to the flow of hot thermal plasma around the disk edges. Energetic superthermal electrons are not the dominant mechanism[15] as evidenced by the low x-ray emission observed above 20 keV.[b] Also, no surface plasma is seen at the rear of wide ($\sim$ 3 mm) foil targets; only the kinetic energy of the accelerated target is observed (Fig. IV.7).

D. Target Motion

The pressure of plasma ablating from the surface of a planar foil target compresses, heats, and moves the foil. Mechanisms that may heat the target are shocks set up by the pressure,[16] thermal conduction of heat from the ablation surface, or deposition of x rays created in the hot ablation plasma. Temperatures of 2-8 eV have been measured at the rear of aluminum foils

---

[a] To ensure uniform irradiation the diameter of the laser spot is chosen to be larger than the diameter of the disk. About 65% of the incident laser energy actually irradiates the disk, remaining intensity variations are $\pm$50%.
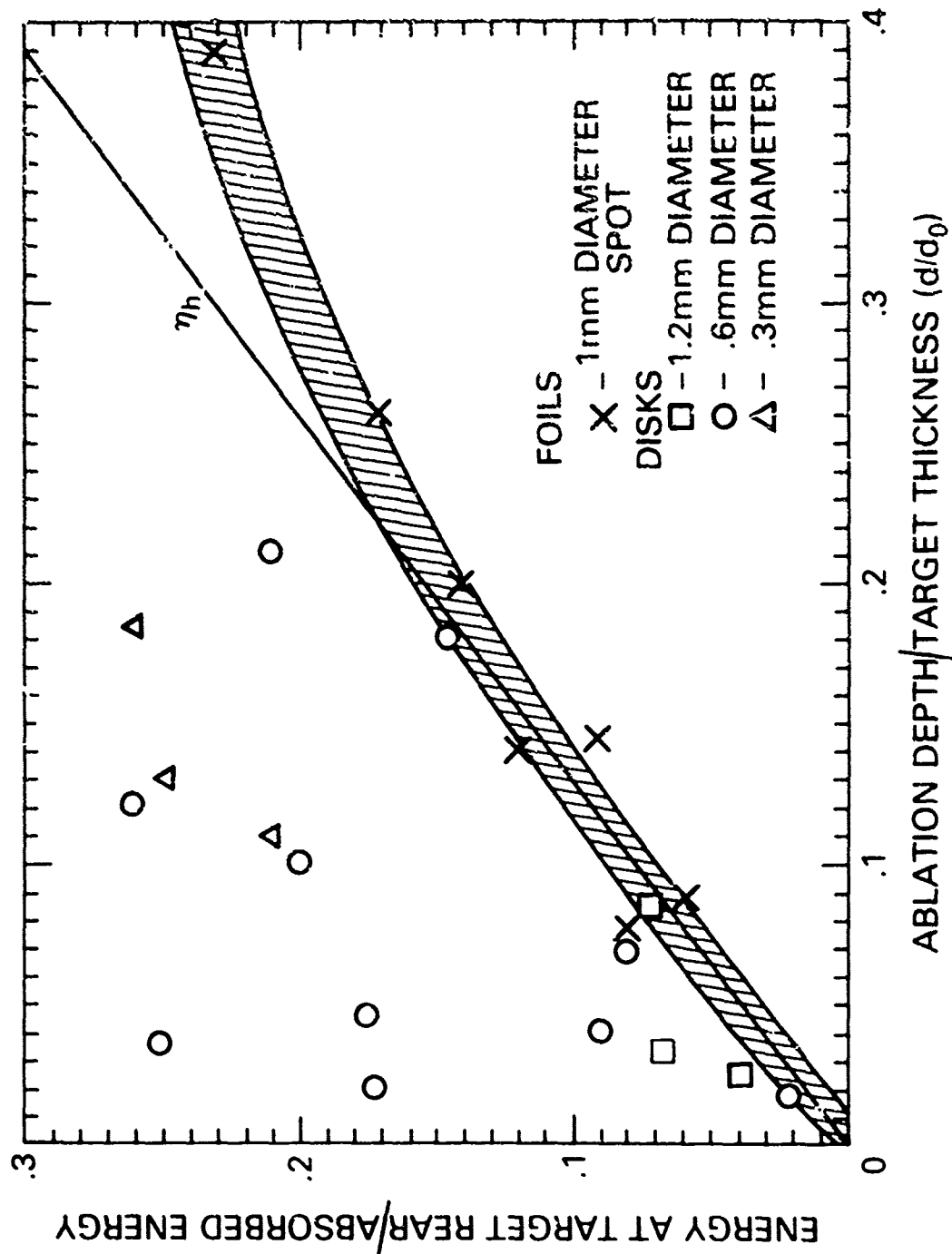[b] Measurement by F. Young

Fig. IV.7. Fraction of absorbed energy at the rear of disk and wide foil targets vs. fraction d/d_o of material ablated from the target surface. The line is the hydrodynamic efficiency of acceleration calculated with the planar rocket model discussed in reference III.6.

irradiated under the conditions of this dissertation and have been ascribed to the latter process.[17] Therefore, the target we accelerate may not be a solid but rather a liquid or a gas or a hopefully well confined plasma. Below, we present evidence that the accelerated target is composed of a high-density, high-pressure region preceded by a low-density, low-pressure region; the velocity of the dense target region is also determined.

a. Double-Foil Shadowgraphy

Figure IV.8a, b, and c shows shadowgrams of a 7μm CH foil target (irradiated at 5×10^{12} W/cm^2) photographed before (a), 1.3 nsec (b), and 3.8 nsec (c) after the peak of the laser pulse. Both Fig. IV.8b and Fig. IV 8c are taken during the same shot. The leading edge of the shadow of the target rear moves about $400\,\mu$m in 2.5 nsec at a speed of 1.6×10^7 cm/sec. Fig. IV.8d, e, and f shows a similar $10\,\mu$m CH foil, under the same irradiance conditions, but with a $7\,\mu$m aluminum impact foil placed $400\,\mu$m behind it. Note that the $10\,\mu$m CH target shadow has already collided with the impact foil 1.3 nsec after the peak of the laser pulse (Fig. IV.8e); but the impact foil does not react immediately! In fact the first sign of the impact foil's reaction occurs only 3.8 nsec after the peak of the laser pulse — more than 2.5 nsec after the collision. Since the impact foil is thin enough so that shock transit time from its front to rear is less than 1.4 nsec (sound speed in cold, uncompressed Al is $\sim 5 \times 10^5$ cm/sec), we interpret the delay as being due to the leading edge of the shadow not exerting enough pressure for the second foil to react. Now, because the pressure exerted by a moving mass is proportional to its density $(\mathscr{P} \propto \rho v^2)$, low pressure implies a low density (for a constant high velocity) and high pressure implies a high density."

Consequently, from the delay in Fig. IV.8e,f over and above the shock transit time and the velocity expected for a shadow of a $10\,\mu$m foil ($\sim 1.1 \times 10^7$ cm/sec) we approximate that

---

"We will show in the next part that the velocity of the shadow edge and the dense target material differ by ~ 2 so that v^2 in the expression $\mathscr{P} \propto \rho v^2$ may be taken as approximately constant
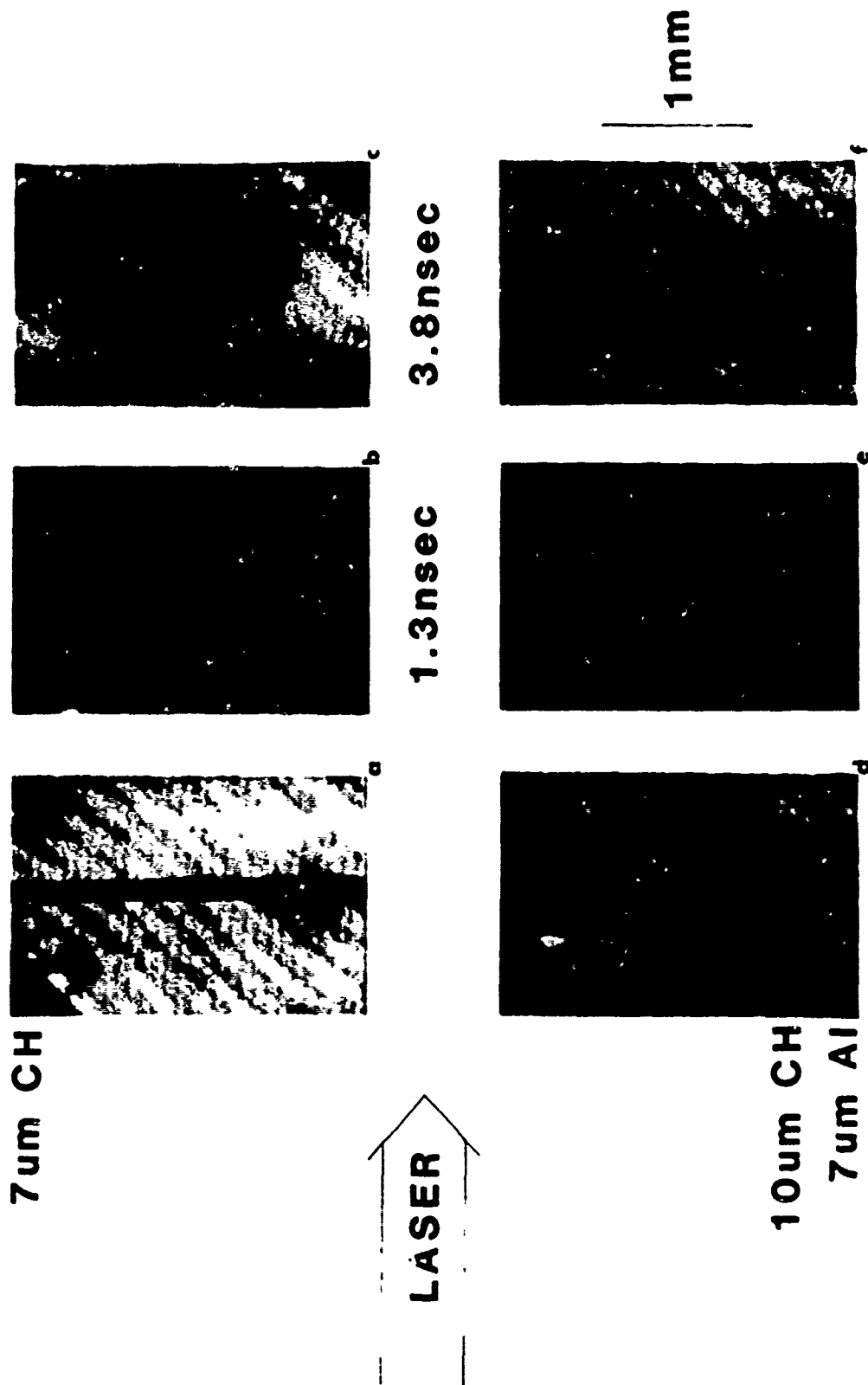
Fig IV.8. Shadowgraphs of single (a,b,c) and double foil targets (d,e,f) irradiated at 5×10^{12} W/cm^2. Photographs b, c, and e, f are taken during the same shot.

R-010

1mm

3.8nsec

1.3nsec

7um CH

10um CH
7um Al

LASER

the leading 100μm of the target shadow consists of low density material unable to exert enough pressure to disturb a 7μm Al foil upon impact. This low density material obscures the main, dense part of the accelerated target from standard shadowgraphy and interferometry diagnostics but is discriminated against here.

b. Double-Foil Streak Photography

A continuous time history of the two foil collision is provided by streak photography. In this technique a cross section of the target and impact foil (Fig. IV.9) is imaged onto a streak camera slit which displaces and records the imaged region in time. The time in which the impact foil's shadow accelerates to its final velocity is short ($\sim$ 0.5 nsec) compared to the laser pulse, which is expected of phenomena associated with the unloading of a shock wave at a free surface. Such phenomena include: motion of the free surface upon decompression, spall from the free surface, or fluff from free surface.[16] We tested for these processes by observing the shadow of yet another, second impact-foil placed behind the first (Fig. IV.10). A long delay ($\sim$ 4 nsec) exists between the collision of the impact-foils and the reaction of the second one. This delay again, is, longer than the shock transit time through either impact foil." Thus, like the leading edge of the ablatively accelerated target, the impact foil is also composed of a high pressure (dense) region preceeded by low pressure (low den. y) material — possibly spall or fluff from the rear of the impact-foil.

Even though the collision between the target and the impact foil is complicated, the sudden reaction of the impact foil makes it a very good time marker for the time at which the dense target material collided with the impact-foil. Fig. IV.11 shows the times at which the impact foil reacts (with respect to an arbitrary origin) for various target-impact-foil separations.

"The target and impact foils in fig IV 10 are made from pyrolytic graphite which is easy to mount flat Similar results were observed for CH targets and aluminum impact foils Shock velocities in pyrolytic graphite were measured by W H. Gust and D A Young (Ref 18) who report velocities between $5 \mu m/ns$ and $11 \mu m/ns$ for pressures between 0 1 and 1 Mbar
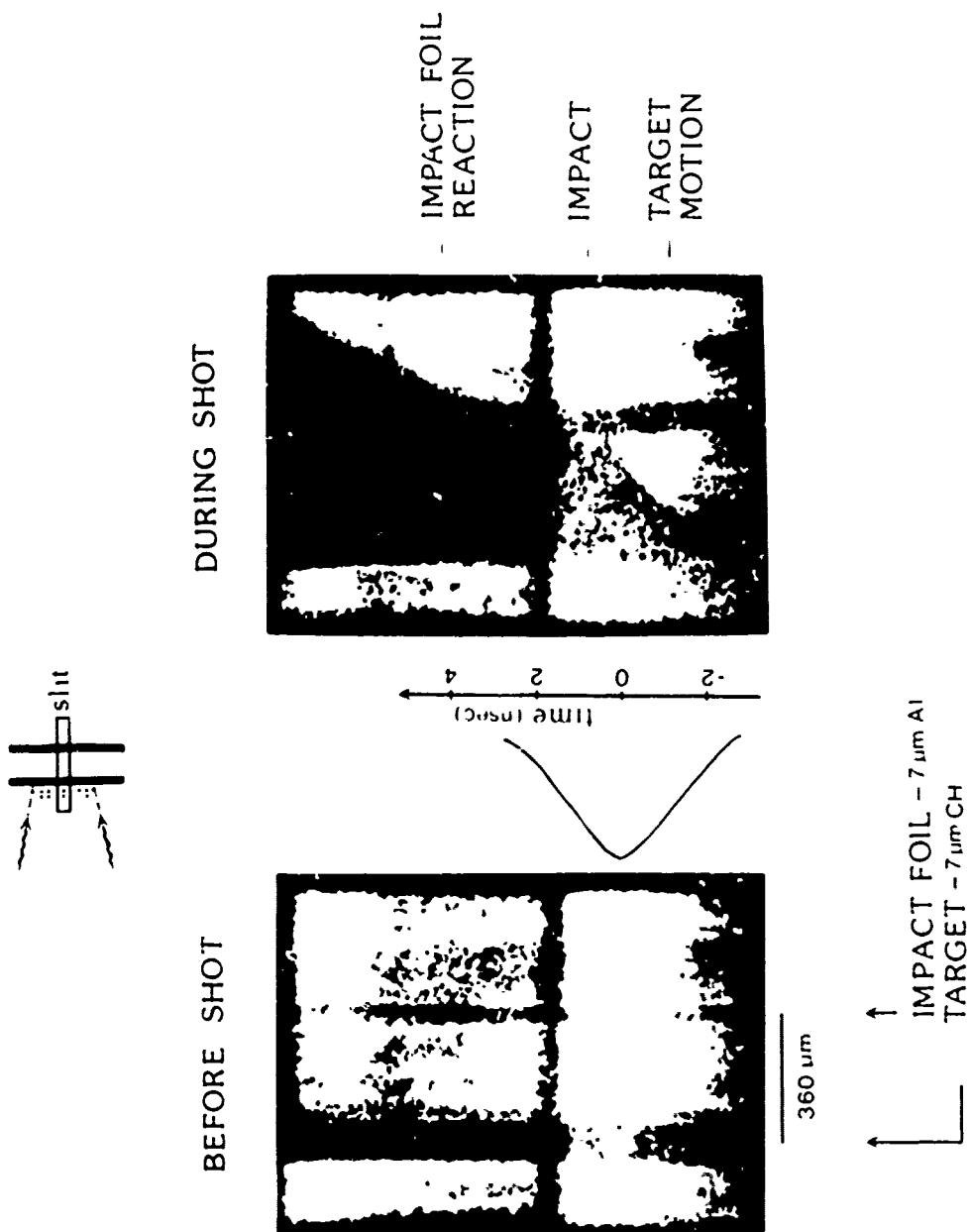
Fig. IV.9. Streaked shadows of a target colliding with an impact foil.

BEFORE SHOT

DURING SHOT

IMPACT FOIL
REACTION

IMPACT

TARGET
MOTION

Time (nsec)

4   2   0   -2

IMPACT FOIL – 7 μm Al
TARGET – 7 μm CH

360 μm

slit

BEFORE SHOT

3 μm C   7μm C

slit

370μm

6.4 nsec

time

2nd IMPACT FOIL REACTS

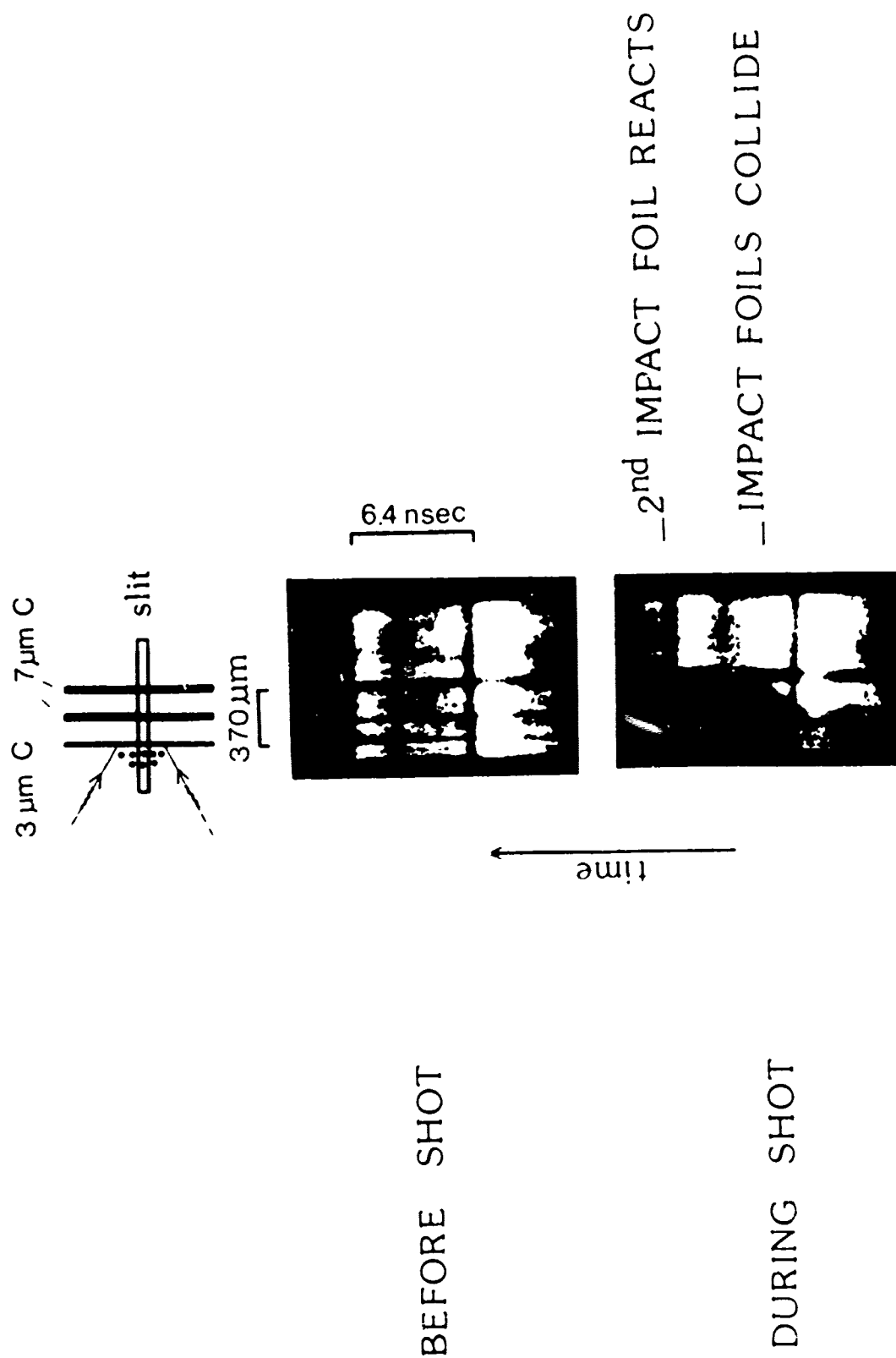IMPACT FOILS COLLIDE

DURING SHOT

Fig IV 10 Triple-foil experiment   A second impact-foil
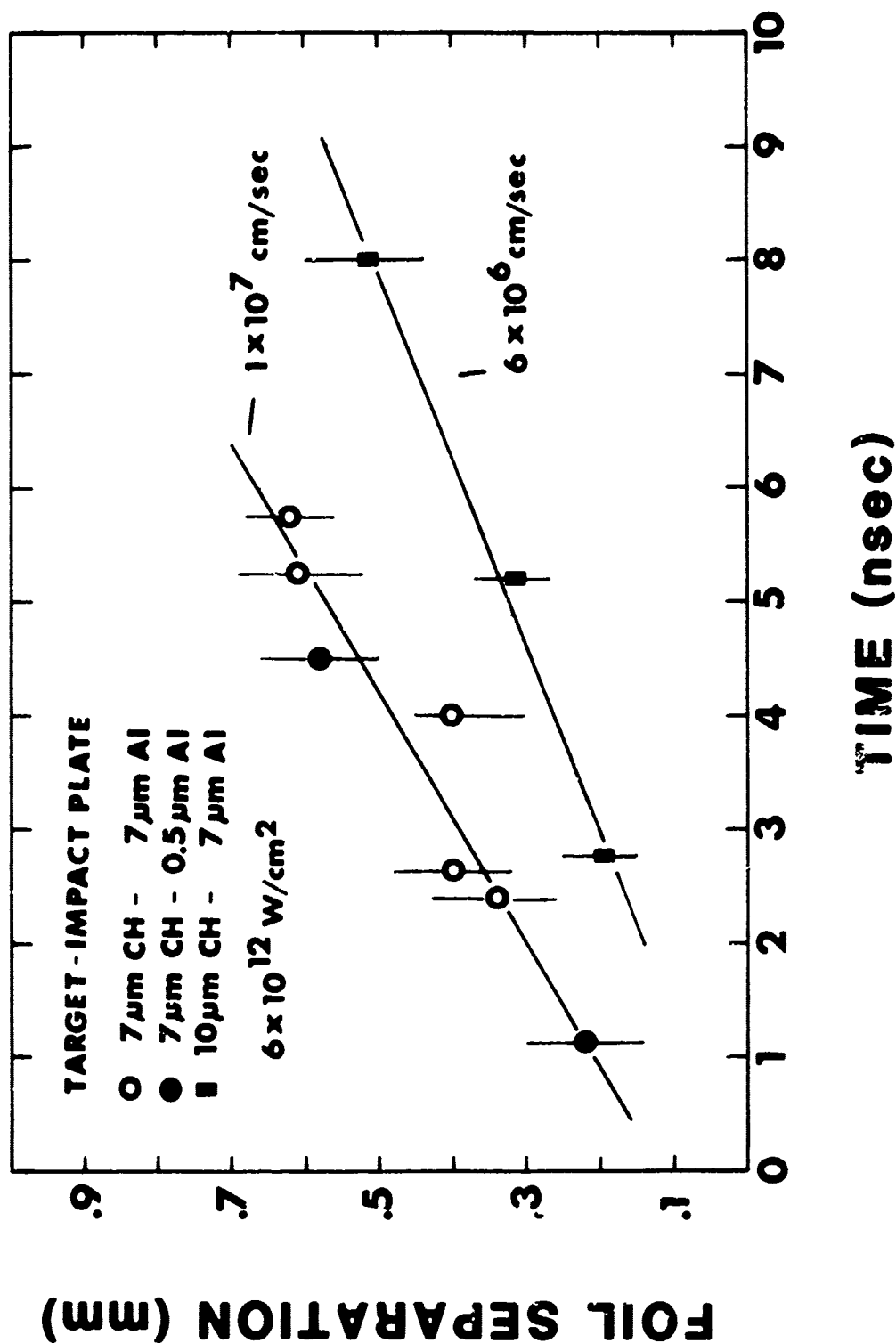diagnoses the first impact-foil

Fig. IV.11. A graph of target-impact foil separation vs the time (with respect to an arbitrary origin) at which the impact-foil reacts to its collission with the target. The slopes of lines drawn thru points accumulated over many shots give the dense target velocities.

For most cases, the separation is large enough so that the collision occurs after much of the ablative acceleration period is over. All the points for each target type lie on a straight line, indicating that no significant spherical expansion of the target in the early stages of its motion takes place; the slope of this line is the velocity of the dense target. At the comparatively low irradiance of 6×10^{12} W/cm^2 we have acce... ~d target foils to 1×10^7 cm/sec — which is near the velocity required for laser fusion. This velocity is also in agreement with that predicted from measurements of the ablation parameters (Figs. IV.4, IV.5) and a simple rocket model.

We have also compared velocities of the dense target material as measured above with the velocities of the shadow of the target rear gotten from the shadow's slope in the double-foil streak pictures. The ratio of the shadow to target velocities is 2 ± 0.8. Consequently, target velocities measured with standard shadowgraphy techniques may infer target velocities that are too high.

CONCLUSION

The characteristics of ablation plasma from planar targets, and the velocities of the abla-
tively accelerated targets were measured. We find that a pressure of ∼10 Mbar is generated at
an absorbed irradiance of 5×10^{11} W/cm^2 and that the pressure scales strongly with irradiance
($\propto I_a^{0.8}$); the hydrodynamic efficiency of acceleration, however, scales weakly with irradiance
Dense target velocities of 100 Km/sec have been measured Thus there exists in this irradiance
regime flexibility in choosing a pellet aspect ratio and irradiance to minimize hydrodynamic ins-
tability and increase smoothing of laser nonuniformities while accelerating shells to fusion-like
velocities. Our results are encouraging for inertial confinement fusion. Other studies that will
help decide the viability of ablatively driven fusion are now being made at NRL

Due to the limited energy of our laser and the large laser-spotsizes required to get quanti-
tative results, the irradiances in our study were limited to below 10^{14} W/cm^2. Studies at higher
irradiances should be made to define the point at which harmful effects such as poor coupling,
production of fast electrons etc. degrade the favorable results we have found thus far Other
target materials and laser wavelengths should be investigated as well. The broadening of the
ion velocity distribution, reported here, deserves further study — possibly with an ion resolving
instrument. Details of the double-foil collision and the conditions between the two foils need
further study to better understand the impulse history of the ablatively accelerated target or to
effectively model a double-shell pellet (to investigate pressur. ⋅ ⋅ : velocity multiplication, for
example).

ACKNOWLEDGMENTS

This work was submitted to the faculty of the University of Maryland in partial fulfillment of the requirements for the degree of Doctor of Philosophy. The experiments were performed at the facilities of the laser-plasma interaction group at the Naval Research Laboratory in Washington, D.C.; it was supported by the Department of Energy and the Office of Naval Research. I am grateful to the entire staff for providing me the opportunity to work in an exciting, stimulating environment.

My thanks to Nick Nocerino for his cheerful and dedicated operation of the laser, Ed Turbyfill for the excellent maintenance of the target facility, and Mort Fink for making many of the targets used in these experiments. The technical assistance of Lori Seymour, Robin McGill, and Hank Hellfeld is appreciated. The dissertation was typed by the Computerized Technical Composition Section of the Technical Information Division at NRL.

I acknowledge helpful discussions with Steve Bodner, B ᐟ Whitlock, John Stamper, Frank Young, John McMahon, Mark Herbst, Bob Lehmberg, and Ed McLean.

Special thanks go to Real Decoste and Steve Obenschain from whom I learned many experimental techniques.

I remain deeply grateful to Barrie Ripin for his guidance and criticism throughout the course of this work. He suggested that I perform the pendulum experiment and use a double-foil to diagnose the target rear (he called it a time resolving pendulum). The advice, encouragement, and continued interest of Hans Griem are likewise appreciated.

Finally, I thank my wife, Yehudit, who played the roles of wife, mother, counselor, worker, housekeeper, and student while my formal education was completed. Her encouragement and unselfish sacrifice made this dissertation possible.

REFERENCES

Section 1

1. For a review of this subject see: H. Motz, " The Physics of Laser Fusion," Chapter 1, Academic Press N.Y. (1979); also J.S. Clarke, H.N. Fisher, and R.J Mason, Phys. Rev. Lett. **30**, 89 (1973); J. Nuckolls, "Laser Interaction and Related Phenomena," Vol. 3, Plenum Press (1974); K.A. Brueckner and S. Jorna, Rev. Mod. Phys. **46**, 325 (1974); G.S. Fraley, E.J. Linnebur, R.J. Mason, and R.L. Morse, Phys. Fluids 1?, 474 (1974).

2. J.D. Lawson, Proc. Phys. Soc. (London) **B70**, 6 (1957).

3. J.H. Nuckolls, L. Wood, A. Thiessen, and G. Zimmerman, Nature **239**, 139 (1972)

4. J.H. Nuckolls, R.O. Bangerter, J.D. Lindl, W.C. Mead, and Y.L. Pan, European Conference on Laser Interaction with Matter, Oxford, England, Sept. 1977 (unpublished)

5. G. Taylor, Proc. Roy. Soc. (London) **A201**, 192 (1950)

6. B.H. Ripin, F.C. Young, J.A. Stamper, C.M. Armstrong, R. Decoste, E.A. McLean, and S.E. Bodner, Phys., Rev. Lett. **39**, 611 (1977)

7. R.C. Malone, R.L. McCrory, and R.L. Morse, Phys. Rev. Lett. **34**, 721 (1975).

8. B.H. Ripin, P.G. Burkhalter, F.C. Young, J.M. McMahon, D.G. Colombant, S.E. Bodner, R.R. Whitlock, D.J. Nagel, D.J. Johnson, N.K. Winsor, C.M. Dozier, R.D. Bleach, J.A. Stamper, and E.A. McLean, Phys. Rev. Lett. **34**, 1313 (1975)

9. W.M. Manheimer, D.G. Colombant, and B.H. Ripin, Phys. Rev. Lett. **38**, 1135 (1977)

10. R. Decoste and B.H. Ripin, Phys. Rev. Lett. **40**, 34 (1978)

11. M.D. Rosen, D.W. Phillion, V.C. Rupert, W.C. Mead. W.L. Kruer, J.J. Thomson, H.N. Kornblum, V.W. Slivinsky, G.J. Caporaso, M.J. Boyle, and K.G. Tirsell, Phys. Fluids 22, 2020 (1979)

12. S.E. Bodner, B.H. Ripin, and J.M. McMahon, Bull. Am. Phys. Soc. 24, 1074 (1979)

13. R. Decoste, S.E. Bodner, B.H. Ripin, E.A. McLean, S.P. Obenschain, and C.M. Armstrong, Phys. Rev. Lett. 42, 1673 (1979)

Section II

1. Absorption, plasma temperature, and related subjects are discussed in: B.H. Ripin, R.R. Whitlock, F.C. Young, S.P. Obenschain, E.A. McLean, and R. Decoste, Phys. Rev. Lett. 43, 350 (1979)

2. Temperature at the rear of the accelerated target was measured by: E.A. McLean, S.H. Gold, J.A. Stamper, R.R. Whitlock, H.R. Griem, S.P. Obenschain, B.H. Ripin, S.E. Bodner, M.J. Herbst, S.J. Gitomer, and M.K. Matzen, Phys. Rev. Lett. 45, 1246 (1980).

3. For experiments on the effect that laser-beam nonuniformities have on target acceleration see: S.P. Obenschain, J. Grun, and B.H. Ripin, Bull. Am. Phys. Soc. 25, 932 (1980); (also to be published)

4. J.L. Bobin, Phys. Fluids 14, 2341 (1971)

5. E. Cojocaru, and P. Mulser, Plasma Phys. 17, 393 (1975)

6. D.V. Giovanelli, and R.P. Godwin, Am. J. Phys. 43, 808 (1975)

7. L. Spitzer, "Physics of Fully Ionized Gases," Wiley (Interscience), New York (1967)

8. J. Dawson, P. Kaw, and B. Green, Phys. Fluids **12**, 875 (1969)

9. R.E. Kidder, Nuclear Fusion **8**, 3 (1968)

10. A. Caruso, and R. Gratton, Plasma Phys. **10**, 867 (1968)

11. T.R. Jarboe, W.B. Kunkel, and A.F. Lietzke, Phys. Fluids **19**, 1501 (1976).

12. B. Ahlborn, and M.H. Key, University of British Columbia Lab Report #73, February 1980.

13. B. Ahlborn, and J.D. Strachan, Can. J. Phys. **51**, 1416 (1973)

14. H. Puell, Z. Naturforsch **25a**, 1807 (1970)

15. I.V Nemchinov, J. Appl. Math. Mech. **31**, 320, (1967); for related work see also: Yu.V. Afanas'ev, E.G. Gamalii, and V.B. Rozanov, Sov. Phys. JETP **44**, 311 (1977); N.G. Basov, V.A. Gribkov, O.N. Krokhin, and G.V. Sklizkov, Sov. Phys. JETP **27**, 575 (1968).

16. S.J. Gitomer, R.L. Morse, and B.S. Newberger, Phys. Fluids **20**, 234 (1977); scaling with irradiance of the mass ablation rate may be determined from this paper if r_s (sonic radius) is assumed to be constant—S.J. Gitomer (private communication)

17. M.D. Rosen, D.W. Phillion, V.C. Rupert, W.C. Mead, W.L. Kruer, J.J Thomson, H.N. Kornblum, V.W. Slivinsky, G.J. Caporaso, M.J. Boyle, and K.G. Tirsell, Phys. Fluids **22**, 2020 (1979)

18. C E. Max, C.F. McKee, and W.C. Mead, Phys. Rev. Lett. **45**, 28 (1980)

19. This discussion is based on reference 13 and citations therein to which the reader is referred for more details.

20. Ya. B. Zel'dovich, and Yu.P. Raizer, "Physics of Shock Waves and High-Temperature Hydrodynamic Phenomena," Vol. II, pg. 676, Academic Press NY (1966)

21. R. Resnick, and D. Halliday, "Physics," Vol. I, pg. 178, J. Wiley NY (1978)

22. R. Decoste, S.E. Bodner, B.H. Ripin, E.A. McLean, S.P. Obenschain, and C.M. Armstrong, Phys. Rev. Lett. **42**, 1673 (1979)

23. Iu. V. Afanas'ev, E.G. Gamalii, O.N. Krokhin, and V.B. Rozanov, Journal of Applied Mathematics and Mechanics, **39**, 427 (1975)

24. R.E. Kidder, Nuclear Fusion **16**, 3 (1976); D E.T.F. Ashby, Nuclear Fusion **16**, 231 (1976)

25. N.G. Kovalskij, M.T. Pergament, and P.P. Pashinin, presented at the IAEA Meeting, San Francisco, CA, Jan. 1978

26. B.H. Ripin, R. Decoste, S.P. Obenschain, S.E. Bodner, E.A. McLean, F.C. Young, R.R. Whitlock, C.M. Armstrong, J. Grun, J.A. Stamper, S.H. Gold, D.J. Nagel, R.H. Lehmberg, and J.M. McMahon, Phys. Fluids **23**, 1012 (1980); Also B.H. Ripin, et. al., Bull. Am. Phys. Soc. **23**, 785 (1978); R.R Whitlock, et. al., ibid.; R. Decoste, et. al., ibid; S.P. Obenschain, et. al., ibid.; E.A. McLean, et. al., ibid.; C.M. Armstrong, et. al., ibid.

27. Y. Kitagawa, H. Nishimura, H. Azehi, M. Miyanaga, K. Yamada, Y. Kato, M. Yokoyama, and C. Yamanaka, presented at the 10th Annual Anomalous Absorbtion Conference, San Francisco, 1980

28. C.G.M. van Kessel, Z. Naturforsch **30**, 1581 (1975)

29. M.H. Key, R.G. Evans, P T. Rumsby, W. Toner, C.L.S. Lewis, M.J. Lamb, A. Moore, I.M. Ward, F. Cunnincham, J.D. Kilkenny, S. Veats, and R.L. Cooke, Presented at the Topical Meeting on Inertial Confinement Fusion in San Diego—1980

30. R. Decoste, B.H. Ripin, J. Grun, J.A. Stamper, S.E. Bodner, S.P. Obenschain, and F.C. Young, Bull. Am. Phys. Soc. **24**, 1074 (1979)

31. S.R. Gunn, and V.C. Rupert, Rev. Sci. Instr. **48**, 1375 (1977): (B.H. Ripin—private communication)

32. See for example: R. Decoste. NRL Memo 3774, April 1978.

33. J.P. Anthes, M.A. Gusinow, and M.K. Matzen, Phys. Rev. Lett. **41**, 1300 (1978).

34. H. Opower, W. Kaiser, H. Puell, and W. Heinicke, Z. Naturforschg. **22**, 1392 (1967)

35. H. Puell, H.J. Neusser, and W. Kaiser, Z. Naturforsch. **25**, 1815 (1970)

36. R. Sigel, Z. Naturforsch, **25**. 488 (1970)

37. J. Grun, S.P. Obenschain, B.H. Ripin, R. Decoste, and M.J. Herbst, presented at the 10th Annual Anomalous Absorption Conference, San Francisco 1980; S.P. Obenschain, J. Grun, J.A. Stamper, and B.H. Ripin, ibid.

38. B. Arad, S. Eliezer, Y. Gazit, H.M. Loebenstein, A. Zigler, H. Zmora, and S. Zweigenbaum, J. Appl. Phys. **50**, 6817 (1979)

39. S. Zweigenbaum, Y. Gazit, and Y. Komet, Plasma Phys. **19**, 1035 (1977)

40. J. Grun, B.H. Ripin, R. Decoste, and S.P. Obenschain, Bull. Am. Phys. Soc. **24**, 1074 (1979)

41. S.P. Obenschain, R.H. Lehmberg, and B.H. Ripin, NRL Memo 4309, Aug. 1980, (Submitted for publication)

Section III

1. J.M. McMahon, and R.H. Lehmberg, to be published in a special issue of the IEEE Journal of Quantum Electronics, Aug. 1981.

2. B.H. Ripin in NRL Memo 3315, Ch. II, (August 1976), (ed. S.E. Bodner).

3. For example: NRL Laser-Plasma Interaction group, NRL Memo 3890, December 1978

4. Apollo Lasers Inc., Los Angeles, California

5. S.R. Gunn, Lawrence Livermore Lab. Report UCID-17308 (1976).

6. B.H. Ripin, R. Decoste, S.P. Obenschain, S E. Boᵤ ᵤer, E.A. McLean, F.C. Young, R.R. Whitlock, C.M. Armstrong, J. Grun, J.A. Stamper, S.H. Gold, D.J. Nagel. R.H. Lehmberg, and J.M. McMahon, Phys. Fluids 23, 1012 (1980)

7. S.P. Obenschain, E.A. McLean and S.H. Gold, NRL Memo 4319, Aug. 1980, (submitted for publication)

8. S.P. Obenschain, J. Grun, and B.H. Ripin, Bull. Am. Phys. Soc. 25, 932 (1980); (also to be published)

9. E.A. Mclean, S.H. Gold, J.A. Stamper, R.R. Whitlock, H.R. Griem, S.T. Obenschain, B.H. Ripin, S.E. Bodner, M.J. Herbst, S.J. Gitomer, and M.K. Matzen, Phys. Rev. Lett. 45, 1246 (1980).

10. F.C. Young in NRL Memo 3591, (1977), (ed. S.E. Bodner)

11. B.H. Ripin, in NRL Memo 3315 pg. 20, (1976), (ed. S.E. Bodner)

12. M. Kaminsky, "Atomic and Ionic Impact Phenomena on Metal Surfaces," Academic Press, New York (1965)

13. K.H. Krebs, Fortschritte der Physik **16**, 419 (1968)

14. R. Decoste, and B.H. Ripin, J. Appl. Phys. . 1503 (1979)

15. These calorimeters, built by B.H. Ripin, are similar to those described by: A. Williams, in 1975 LASL Annual Report No. LA-6050-PR, 82, (1976) (ed. F. Skoborne).

16. B.H. Ripin, F.C. Young, J.A. Stamper, C.M. Armstrong, and R. Decoste, Phys. Rev. Lett. **39**, 611 (1977)

17. A calorimeter design somewhat different from ours is presented by: S.R. Gunn, and V.C. Rupert, Rev. Sci. Instrum. **48**, 1375 (1977).

18. X-ray measurements above 1 KeV are given on pg. 15 of Ref. 3 and in Ref. 6 above.

19. Measurements on targets irradiated in ambient air include: J.E. Lowder, and L.C. Pettinghill, Appl. Phys. Lett **24**, 204 (1974); A.N. Pirri, R. Schlier, and D. Northam, Appl. Phys. Lett. **21**, 79 (1972); S.A. Metz, Appl. Phys. Lett. **22**, 211 (1973); S.A. Metz, L.R. Hettche, R.L. Stegman, and J.T. Schriempf, J. Appl. Phys **46**, 1634 (1975); L.R. Hettche, J.T. Schriempf, and R.L. Stegman, J. Appl. Phys. **44**, 4079 (1973).

20. D.W. Gregg, and S.J. Thomas, J. Appl. Phys. **37**, 2787 (1966)

21. S. Zweigenbaum, Y. Gazit, and Y. Komet, Plasma Phys. **19**, 1035 (1977)

22. B. Arad, S. Eliezer, Y. Gazit, H.M. Loebenstein, A. Zigler, H. Zmora, and S. Zweigenbaum, J. Appl. Phys. **50**, 6817 (1979)

23. B. Arad, S. Eliezer, S. Jackel, A. Krumbein, H.M. Loebenstein, D. Salzmann, A. Zigler, H. Zmora, and S. Zweigenbaum, Phys. Rev. Lett. **44**, 326 (1980)

24. R.F Benjamin, G.H. McCall, and A.W. Ehler, Phys. Rev. Lett. **42**, 890 (1979)

25. B.H. Ripin, S.P. Obenschain, J. Grun, M.J. Gerbst, E.A. Mclean, J.A. Stamper, R.R. Whitlock, J.M. McMahon, and S.E. Bodner, Bull. Am. Phys. Soc. **25**, 946 (1980)

Section IV

1. S. Zweigenbaum, Y. Gazit, and Y. Komet, Plasma Phys. **19**, 1035 (1977)

2. S.P. Obenschain, J. Grun, and B.H. Ripin, Bull. Am. Phys. Soc. **25**, 932 (1980); (also to be published)

3. R.E. Kidder, Nuclear Fusion **8**, 3 (1968)

4. A. Caruso, and R. Gratton, Plasma Phys. **10**, 867 (1968)

5. H. Puell, Z. Naturforsch **25a**, 1807 (1970)

6. B. Ahlborn, and M.H. Key, University of British Columbia Lab. Report #73, February 1980

7. T.R. Jarboe, W.B. Kunkel and A.F. Lietzke, Phys. Fluids **19**, 1501 (1976).

8. S.J. Gitomer, R.L. Morse, and B.S. Newberger, Phys. Fluids **20**, 234 (1977); Scaling of the mass ablation rate may be determined from this paper if r_s (the sonic radius) is assumed constant-S.J. Gitomer (private communication)

9. I.V. Nemchinov, J. Appl. Math. Mech. **31**, 320 (1967)

10. C.E. Max. C.F. McKee, and W.C. Mead, Phys. Rev. Lett. **45**, 28 (1980)

11. For a review of self-generated magnetic fields see J.A. Stamper, NRL Memo 3872, (1978); J.A. Stamper, E.A. McLean, and B.H. Ripin, Phys. Rev. Lett. **40**, 1177 (1978)

12. L. Montierth, and R.L. Morse, presented at the Eighth Annual Conference on Anomalous Absorption of Electromagnetic Waves, Tucson, Arizona, April 1978

13. H. Puell, H.J. Neusser, and W. Kaiser, Z. Naturforsch 25a, 1815 (1970)

14. J.P. Anthes, M.A. Gusinow, and M.K. Matzen, Phys. Rev. Lett. 41, 1300 (1978)

15. N.A. Ebrahim, C. Joshi, D.M. Villeneuve, N.H. Burnett, and M.C. Richardson, Phys Rev. Lett. 43, 1996 (1979)

16. Ya. B. Zeldovich, and Yu. P. Raizer, "Physics of Shock Waves and High-Temperature Hydrodynamic Phenomena", Academic Press, New York (1967)

17. E.A. McLean, S.H. Gold, J.A. Stamper, R.R. Whitlock, H.R. Griem, S.P. Obenschain, B.H. Ripin, S.E. Bodner, M.J. Herbst, S.J. Gitomer, and M.K. Matzen, Phys. Rev. Letters 45, 1246 (1980)

18. W.H. Gust and D.A. Young in "High Pressure Science and Technology," Volume 1, pg. 944, Plenum Press, New York (1979)

DISTRIBUTION LIST

USDOE (50 copies)
P.O. Box 62
Oak Ridge, TN 37830

National Technical Information Service (24 copies)
U.S. Department of Commerce
5285 Port Royal Road
Springfield, VA 22161

NRL, Code 2628 (35 copies)

NRL, Code 4730 (100 copies)

NRL, Code 4700 (25 copies)

USDOE (6 copies)
Office of Inertial Fusion
Washington, D.C.
Attn: Dr. G. Canavan
      Dr. R. Schriever
      Dr. S. Kahalas
      Dr. T. Godlove
      Dr. K. Gilbert

Lawrence Livermore Laboratory
P.O. Box 808
Livermore, CA 94551
Attn: Dr. D. Attwood, L481
      Dr. W. Kruer, L545
      Dr. B. Lasinski
      Dr. C. Max, L545
      Dr. A. Glass
      Dr. . Coleman
      Dr. J. Nuckolls
      Dr. W. Mead
      Dr. N. Ceglio
      Dr. R. Kidder

INTERNAL DISTRIBUTION

Code 4790 Dr. D. Colombant
           Dr. W. Manheimer

Department of Physics and Astronomy
University of Maryland
College Park, MD 20740
Attn: Dr. H. Griem

Los Alamos Scientific Laboratory
Los Alamos, NM 87545
Attn: Dr. R. Godwin
      Dr. D. Giovanielli
      Dr. J. Kindel, Dr. D. Forslund

University of Rochester
Rochester, NY 14627
Laboratory for Laser Energetics
Attn: Dr. R.S. Craxton
      Dr. W. Seka

KMS Fusion
3941 Research Park Drive
P.O. Box 1567
Ann Arbor, MI 48106
Attn: Dr. F. Mayer

Institut fur Plasmaphysik
8046 Garching
Bei Munchen
West Germany
Attn: Dr. R. Sigel
      Dr. H. Takabe c/o Dr. P. Mulser
National Research Council
Division of Physics
100 Susser Drive
Ottawa K1A-OR6, Canada
Attn: Dr. J. Alcock

University of Quebec
INRS Energie
Case Postale 1020
Varennes, Quebec
Attn: Dr. T. Johnston
      Dr. R. Decoste

Rutherford Laboratory
Chilton, Didcot
Oxon OX110QX
England
Attn: Dr. M. Key
      Dr. R. Evans

85

Sandia Laboratory
Albuquerque, NM
Attn: Dr. K. Matzen
      Dr. J. Anthes
      Dr. R. Palmer

Institute for Laser Engineering
Osaka University
Suita Osaka, 565
Japan
Attn: Dr. C. Yamanaka

Shanghai Institute of Optics and Fine Mechanics
Academia Sinica
Shanghai, PRC
Attn: Prof. Gan Fu-xi
      Prof. Yu Wen-yan
      Prof. Xu Zhi-zhan
      Prof. Deng Xi-ming
      Prof. Tan Wei-han
      Mr. Pan Cheng-min

Soreq Nuclear Center
Yavne, Israel
Attn: Dr. A. Krumbein

INTERNAL DISTRIBUTION

Code 4040   J. Boris
            J. Gardener
            J. Orens

Sergio Morosi
Ist. Fisica Applicata
via Bassi 6 Pavia - ITALY

Defense Technical Information Center
Cameron Station
5010 Duke Street
Alexandria, VA 22314

Prof. G. Wallis
Prof. Klaus Junge
Zentralinstitut fur Optik und Spektroskopie
DDR-1199 Berlin-Adlershof
Rudower Chaussee 6
West Germany

J. Balmer
Institute of Applied Physics
Sidlerstr. 5
CH-3012 BERN/Switzerland

Hn Qiouan
Lab. de Physique des Lasers
Uni. Paris Nord
93430 Villetaneuse/FRANCE

Gl. Barifi
Istituto Fisica Application
Universita di Paria
Pavia 27100 Italy

N.A. Tahir
Dept. of Nat. Phil
Glasgow University
Glasgow G12 (U.K.)

B. Meyer
HDE
CE_
BP27
94190 Villeneuve St. Georges
FRANCE

D. Unaugst
University of Jena
6900 Jena
Schlobgassel
Germ. Dem. Rep.

Patrick Flynn
Bldg. 1
Atomic Weapons Research Estab
Aldermaston
Reading, U.K.

N. Kovalsky
Kurchatov Institute of Atomic
    Energy
D-182 Moscow USSR

J. Virmont
Ecole Polytechnique Gzeco ILM
Palaiseau 91127
FRANCE

86